The Astrophysical Journal, 645:1246–1263, 2006 July 10

THE *SPITZER* c2d SURVEY OF LARGE, NEARBY, INTERSTELLAR CLOUDS. III. PERSEUS OBSERVED WITH IRAC

Jes K. Jørgensen,[1] Paul M. Harvey,[2] Neal J. Evans II,[2] Tracy L. Huard,[1] Lori E. Allen,[1] Alicia Porras,[1] Geoffrey A. Blake,[3] Tyler L. Bourke,[1] Nicholas Chapman,[4] Lucas Cieza,[2] David W. Koerner,[5] Shih-Ping Lai,[4] Lee G. Mundy,[4] Philip C. Myers,[1] Deborah L. Padgett,[6] Luisa Rebull,[6] Anneila I. Sargent,[7] William Spiesman,[2] Karl R. Stapelfeldt,[8] Ewine F. van Dishoeck,[9] Zahed Wahhaj,[5] and Kaisa E. Young[2]

Received 2006 January 27; accepted 2006 March 17

ABSTRACT

We present observations of 3.86 deg^2 of the Perseus molecular cloud complex with the *Spitzer Space Telescope* Infrared Array Camera (IRAC). The maps show strong extended emission arising from shocked H_2 in outflows and from polycyclic aromatic hydrocarbon features. More than 120,000 sources are extracted toward the cloud. Based on their IRAC colors and comparison to off-cloud and extragalactic fields, we identify 400 candidate young stellar objects. About two-thirds of these are associated with the young clusters IC 348 and NGC 1333, while the last third is distributed over the remaining cloud. The young stellar objects are classified according to the slope of their spectral energy distributions. Significant differences are found between the numbers of embedded Class I objects and more evolved Class II objects in IC 348, NGC 1333 and the remaining cloud, with the embedded Class I and "flat-spectrum" YSOs constituting 14%, 36% and 47% of the total number of YSOs identified in each of these regions. The high number of Class I objects in the extended cloud (61% of the Class I objects in the entire cloud) suggests that a significant fraction of the current star formation occurs outside the two main clusters. Finally, we discuss a number of outflows and identify their driving sources, including the deeply embedded Class 0 sources outside the two main clusters. The Class 0 objects are detected by *Spitzer* and have very red [3.6] − [4.5] colors, but they do not show similarly red [5.8] − [8.0] colors. The Class 0 objects are easily identifiable in color-color diagrams but are problematic to extract automatically due to the extended emission from shocked gas or scattered light in cavities related to the associated outflows.

Subject headings: infrared: stars — ISM: clouds — stars: formation

1. INTRODUCTION

Low-mass stars such as our own Sun are formed in a wide range of different environments, ranging from isolated cores to large, dense clusters. To fully understand the differences in the formation processes among these environments, large unbiased surveys and compilations of young stellar objects are necessary. A major goal of the *Spitzer Space Telescope* legacy project "From Molecular Cores to Planet Forming Disks" (c2d; Evans et al. 2003) is to characterize star formation in a variety of environments through a combination of mapping and spectroscopic observations utilizing the full palette of *Spitzer* instruments.

The Perseus molecular cloud is a prime example of a low-mass star-forming region. Low-mass protostars are found in a number of dense clusters, such as NGC 1333 and IC 348, looser groups associated with smaller dark clouds, including Barnard 1, Barnard 5, L1448 and L1455, and a number of dense cores. Although no massive stars are currently formed in the cloud, OB stars have been formed previously in the vicinity, as witnessed by the Per OB2 association (e.g., de Zeeuw et al. 1999). This paper presents *Spitzer* Infrared Array Camera (IRAC) maps of 3.86 deg^2 of Perseus from the c2d legacy project. This paper is the third in a series of papers presenting the basic results for the five large clouds in the c2d survey. The two previous papers in this series presented MIPS (Multiband and Imaging Photometer for *Spitzer*) observations of Chamaeleon (Young et al. 2005) and IRAC observations of Serpens (Harvey et al. 2006). We present the results for all clouds in a fairly standard format to facilitate comparisons. While this paper is based on IRAC data, some information from MIPS observations of Perseus by c2d (L. Rebull et al. 2006, in preparation) is used in source classification and in discussion of particular sources.

Perseus was first mapped, in full, in CO by Sargent (1979). Ladd et al. (1993) identified 23 candidate young stellar objects (YSOs) from the *IRAS* (*Infrared Astronomical Satellite*) Point-Source Catalog and surveyed these at 2 μm. Ladd et al. found that the YSO candidates were distributed throughout the cloud, with higher numbers toward the prominent clusters in IC 348 and NGC 1333: 87% of the YSOs were located within 1° of these two clusters, but only 30% within 30′. Subsequent near-infrared studies have focused on the regions around NGC 1333 (Lada et al. 1996; Wilking et al. 2004) and IC 348 (Lada & Lada 1995; Luhman et al. 2003), identifying a large number of infrared-excess sources (about 60 sources in each region, corresponding

[1] Harvard-Smithsonian Center for Astrophysics, 60 Garden Street MS42, MA 02138, jjorgensen@cfa.harvard.edu.
[2] Department of Astronomy, University of Texas at Austin, 1 University Station C1400, Austin, TX 78712.
[3] Division of Geological and Planetary Sciences, MS 150-21, California Institute of Technology, Pasadena, CA 91125.
[4] Department of Astronomy, University of Maryland, College Park, MD 20742.
[5] Department of Physics and Astronomy, Northern Arizona University, NAU Box 6010, Flagstaff, AZ 86011-6010.
[6] *Spitzer* Science Center, MC 220-6, California Institute of Technology, Pasadena, CA 91125.
[7] Division of Physics, Mathematics, and Astronomy, MS 105-24, California Institute of Technology, Pasadena, CA 91125.
[8] Jet Propulsion Laboratory, MS 183-900, California Institute of Technology, Pasadena, CA 91125.
[9] Leiden Observatory, PO Box 9513, NL 2300 RA Leiden, Netherlands.

to 50% and 20% of the total number of cluster members in NGC 1333 and IC 348, respectively).

The exact distance to Perseus remains uncertain. It is not clear whether the cloud is located in the vicinity of the Per OB2 association (at a distance of 320 pc inferred from *Hipparcos* parallax measurements; de Zeeuw et al. 1999) or whether the cloud is closer, in front of the OB association at 200–250 pc, as suggested by extinction studies (e.g., Černis 1990). Whether a single distance to the entire cloud is valid or whether the Perseus cloud in fact has a distance gradient (similar to an observed line-of-sight velocity gradient; Sargent 1979) or is a conglomeration of smaller clouds is another issue. In any case, following Enoch et al. (2006), a distance of 250 $\pm$ 50 pc is adopted in this paper.

2. OBSERVATIONS

In total, 4.29 deg^2 of Perseus was observed with the IRAC camera in each of four bands at 3.6, 4.5, 5.8 and 8.0 μm on 2004 September 7 and 8. The IRAC camera observes these four bands simultaneously with one field of view imaged by the 3.6 and 5.8 μm filters and a nearby field imaged by the 4.5 and 8.0 μm filters. Mosaics of our Perseus observations overlap in all four IRAC bands in a region covering 3.86 deg^2. The mapped area was selected on the basis of the ^{13}CO maps of Padoan et al. (1999), including the entire region with $A_V \gtrsim 2$ mag. Figure 1 shows an overlay of the observed region on a dust column density map based on *IRAS* 60 and 100 μm thermal emission (Schnee et al. 2005). The cloud was mapped in two epochs to help in the elimination of transient objects such as unknown asteroids. The regions around NGC 1333 and IC 348 were mapped in Guaranteed Time Observations (GTOs; R. A. Gutermuth et al. [2006, in preparation] and Lada et al. [2006], respectively) and observed in one epoch within the c2d program. Two smaller gaps (per_gap1, per_gap2 in Table 1) between the fields mapped by the GTO and c2d were added later and only observed in one epoch. MIPS observations of the Perseus cloud from c2d are discussed in a separate paper (L. Rebull et al. 2006, in preparation).

Furthermore, six off-cloud fields, each of 0.08 deg^2, were observed for statistical comparisons with 0.05 deg^2 overlap between all four IRAC bands. These regions were selected as having a relatively low extinction ($A_V < 0.5$ mag) from the large-scale CO maps by Dame et al. (2001) and chosen to cover a range of Galactic latitudes around Perseus. Table 1 provides a summary of the observations, including the distribution of the on- and off-cloud fields.

3. DATA REDUCTION

The data reduction started from the IRAC basic calibrated data (BCD) images supplied by the *Spitzer* Science Center (SSC) from their S11.4.0 pipeline. The SSC pipeline BCD data are delivered with dark and bias levels subtracted and flat-field–corrected. Instrumental signatures, bad pixels, or pixels saturated by bright sources are furthermore masked. Finally, the BCD images are flux-calibrated into physical units (MJy sr^{-1}). To arrive at the final source catalogs our data reduction continues from the BCD images by (1) correcting additional background and image effects, (2) creating a mosaic from individual frames, (3) extracting sources from the final mosaic, and (4) merging the catalogs across bands. A detailed description of the processing is described in the documentation for the delivery of c2d data (Evans et al. 2005) and further discussed in Harvey et al. (2006).

In the first step, the c2d pipeline improves the BCD images by additional masking of bad pixels not picked up by the SSC pipeline reduction, correcting muxbleed and column pull-down defects occurring near moderately bright sources and finally correcting the so-called first-frame effect for the band 3 (5.8 μm) images (see Harvey et al. 2006 for further discussion of these corrections). In the second step, mosaics are created from the frames from observations in the two different epochs and from short exposure (0.4 s) data. The combination of the two epoch observations eliminates transient effects including most asteroids in the mosaics. The inclusion of the short exposure data allows masking of likely saturated areas in the longer integration frames.

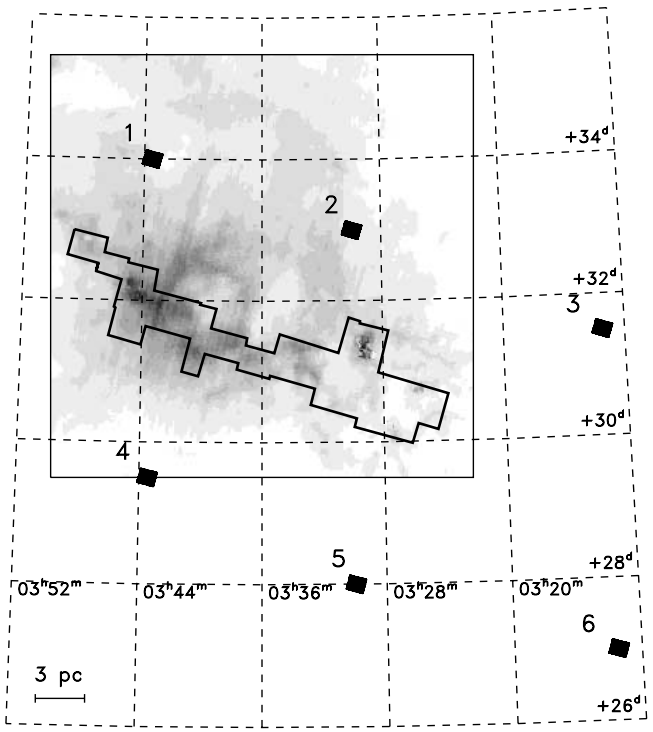

FIG. 1.—Coverage by the c2d IRAC maps. The thick black line indicates the region covered by all four IRAC bands from which the source catalogs are extracted. The off-cloud fields are likewise shown (*black solid fields*) and numbered 1–6. The gray-scale map is the dust column density distribution based on *IRAS* 60 and 100 μm thermal emission from COMPLETE (Schnee et al. 2005) encompassed by the black rectangle. The prominent ring seen in the map of Schnee et al. is not a true column density feature but rather reflects a different, warmer dust population in this region (Ridge et al. 2006).

As a third step, sources are extracted using a c2d developed tool, `c2dphot` (P. Harvey et al. 2006, in preparation), which extracts sources using digitized source profiles and calculates photometry for each source, including uncertainty in the derived fluxes. The source extractor recognizes "small" extended sources (i.e., sources better fit by a two-axis ellipsoid than a point-source profile) and provides an estimate of the size of these. These extended sources (sources with "image type" 2 in the delivered c2d catalogs; Evans et al. 2005) are included in our general catalog with fluxes extracted from aperture photometry. However, we leave them out of the color-color/color-magnitude diagrams and discussions in § 5 and onward in this paper for consistent photometry of sources in our high-quality catalogs (i.e., when comparing unresolved and extended sources). The accuracy of the flux calibration for the sources is estimated to $\approx$15%. The extraction is applied to each of the single-epoch data sets together with the combined mosaics. A uniform flux cutoff of 0.05 mJy is applied across the regions and bands. The source lists from each data set are cross-checked serving as an additional test of transient detections.

TABLE 1
Summary of Observations

Field	Position				AOR (Astronomical Observation Request)	
	α (J2000.0)	δ (J2000.0)	l (deg)	b (deg)	Epoch 1	Epoch 2
AORs Mapped in Two Epochs by c2d						
per_1	03 47 44.0	+32 44 44.0	160.6	−16.9	0005783552	0005790464
per_2	03 46 01.0	+32 29 16.0	160.5	−17.4	0005783808	0005790720
per_4	03 44 53.3	+31 39 00.0	160.9	−18.2	0005784064	0005791232
per_5	03 41 59.0	+31 48 34.0	160.3	−18.4	0005784320	0005791488
per_6	03 40 12.0	+31 26 41.0	160.2	−18.9	0005784576	0005791744
per_7	03 38 27.0	+31 22 11.0	159.0	−19.2	0005784832	0005792000
per_8	03 36 23.0	+31 08 41.0	159.7	−19.7	0005785088	0005792256
per_9	03 33 36.0	+31 08 50.0	159.2	−20.1	0005785344	0005792512
per_10	03 31 00.0	+30 36 36.0	159.1	−20.8	0005785600	0005792768
per_11	03 30 09.0	+31 31 48.0	158.4	−20.2	0005785856	0005793024
per_13	03 28 41.0	+30 34 02.0	158.7	−21.2	0005786112	0005793536
per_14	03 27 12.0	+30 11 49.0	158.7	−21.7	0005786368	0005793792
per_15	03 25 20.0	+30 30 01.0	158.2	−21.6	0005786624	0005794048
per_16	03 27 08.0	+30 39 42.0	158.4	−21.3	0005786880	0005794304
per_17	03 29 39.0	+30 55 28.0	158.7	−20.8	0005787136	0005794560
per_18	03 31 05.0	+31 04 42.0	158.8	−20.4	0005787392	0005794816
AORs Mapped in One Epoch by GTO Team and in One Epoch by c2d						
ic348	03 44 21.5	+32 10 16.8	160.4	−17.8	0003651584	0005790976
ngc1333	03 29 00.6	+31 18 42.9	158.3	−20.5	0003652864	0005793280
AORs to Cover Gaps between c2d and GTO areas, Mapped in One Epoch by c2d						
per_gap1	03 29 45.0	+30 54 50.0	158.7	−20.7	0016034304	...
per_gap2	03 44 36.0	+31 55 38.0	160.7	−17.0	0016034048	...
Off-Cloud Regions Mapped in Two Epochs by c2d						
per_oc1	03 43 30.0	+34 00 00.0	159.1	−16.5	0005795072	0005798912
per_oc2	03 30 00.0	+33 00 00.0	157.4	−19.1	0005795328	0005799168
per_oc3	03 13 30.0	+31 30 00.0	155.3	−22.3	0005795584	0005799424
per_oc4	03 43 30.0	+29 30 00.0	162.1	−20.0	0005795840	0005799680
per_oc5	03 30 00.0	+28 00 00.0	160.7	−23.0	0005796096	0005799936
per_oc6	03 13 30.0	+27 00:00.0	158.1	−26.0	0005796352	0005800192

Note.—Units of right ascension are hours, minutes, and seconds, and units of declination are degrees, arcminutes, and arcseconds.

In the fourth step, the lists are merged by cross-identifying sources from each of the IRAC bands followed by merging with the MIPS 24 μm (L. Rebull et al. 2006, in preparation) and 2MASS catalogs. In the band merging an IRAC source is accepted as identified in two bands if the positional agreement is better than 2.″0. Cross identifications with MIPS 24 μm require positional agreement better than 4.″0 and with 2MASS better than 2.″0.

4. RESULTS

4.1. *Description of the Overall Cloud Environment*

A three-color composite of the Perseus region is presented in Figure 2, showing IRAC bands 1 (IRAC1; 3.6 μm), 2 (IRAC2; 4.5 μm), and 4 (IRAC4; 8.0 μm). For display purposes, the image in this figure does not include the short integration data that are otherwise used for photometry of saturated sources. For comparison, the extinction contours from Enoch et al. (2006) are overlaid on the band 2 image in Figure 3 and prominent regions are identified. Figure 4 shows gray-scale images (logarithmic stretch) of the cloud for each of the IRAC bands. As pointed out above, the field observed by the IRAC1 and IRAC3 bands is offset from the field observed by the IRAC2 and IRAC4 bands, which is clearly seen by comparing the panels of Figure 4. Only the overlap region is shown in Figure 2 and used in the subsequent analysis. The emission seen in the IRAC bands highlight different features of the cloud: band 1 shows the largest fraction of stars; band 2, in particular, is sensitive to H_2 rotational transitions arising in shocked gas associated with the outflows, whereas bands 3 and 4 include emission from the polycyclic aromatic hydrocarbon (PAH) features at 6.2 and 7.7 μm.

Besides the two main clusters, NGC 1333 and IC 348, a striking feature in the image is the Perseus ring (sometimes referred to as G159.6−18.5) in the eastern part of the cloud, which is seen in all bands—most prominently in the 8.0 μm (likely PAH) emission. It has been suggested to be a supernova remnant (Fiedler et al. 1994) or an H II region associated with a late O/early B star, HD 278942 (de Zeeuw et al. 1999; Andersson et al. 2000). Ridge et al. (2006) argue that the shell is located behind the cloud (although it may be "touching" it).

The western part of the cloud shows less PAH emission than the eastern part, but harbors a number of prominent outflows, in particular in the B1, L1448, and L1455 regions (see inserts). We

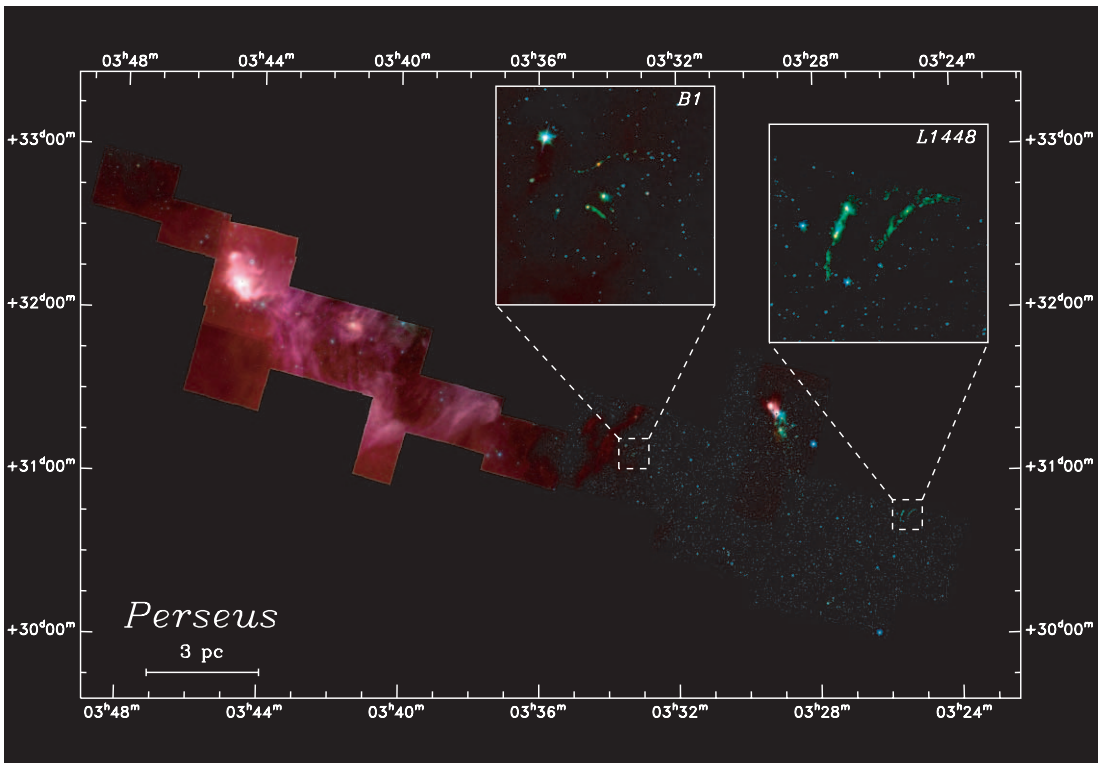

FIG. 2.—Three-color image of the Perseus region with IRAC1 (3.6 μm, *blue*), IRAC2 (4.5 μm, *green*), and IRAC4 (8.0 μm, *red*).

will return to a discussion of some of these outflows in § 6. The extinction map (Fig. 3) demonstrates, however, that regions of medium-high column density are not isolated to a particular part of the cloud. In contrast, the Serpens cloud exhibits smaller and more isolated regions of high extinction, where the highest number of Class I YSOs are also found (Harvey et al. 2006). In Perseus, regions of high extinction are likewise found close to IC 348 and NGC 1333, but these are in no way unique. There is also no clear correlation between the regions of high extinction and the extended emission seen in the IRAC images.

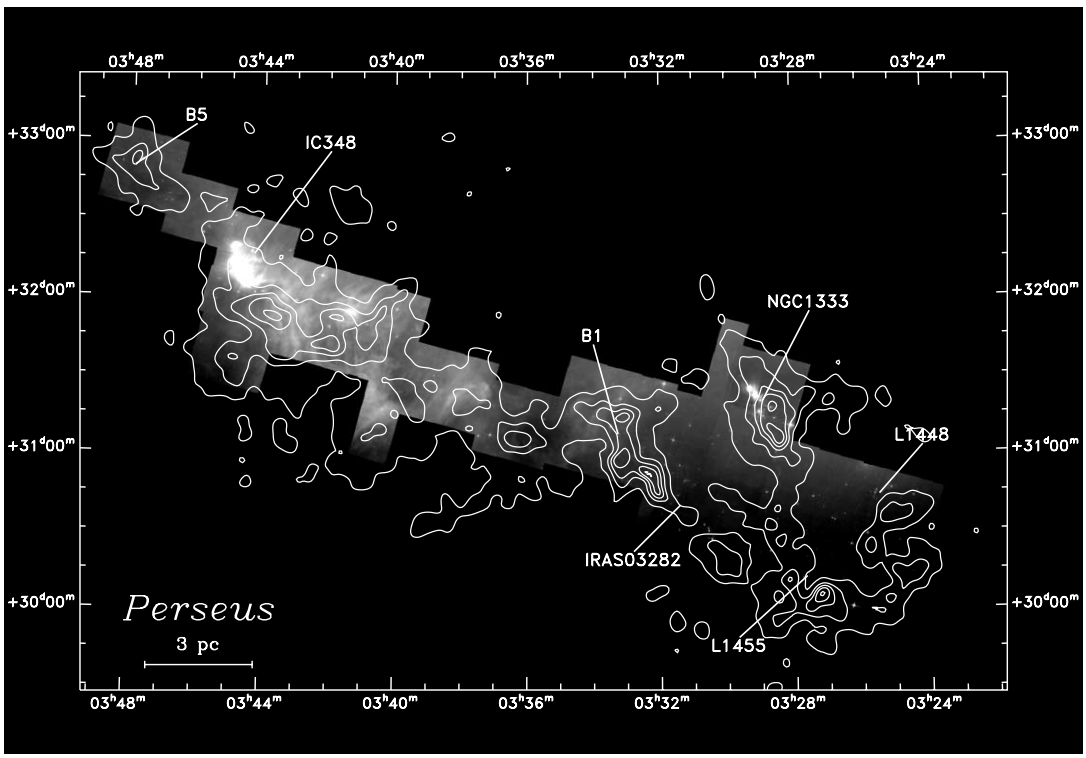

FIG. 3.—IRAC2 image with prominent clusters and cores indicated. The dashed contours indicate an extinction map with levels corresponding to $A_V = 2$, 4, 6, 8, and 10 mag.

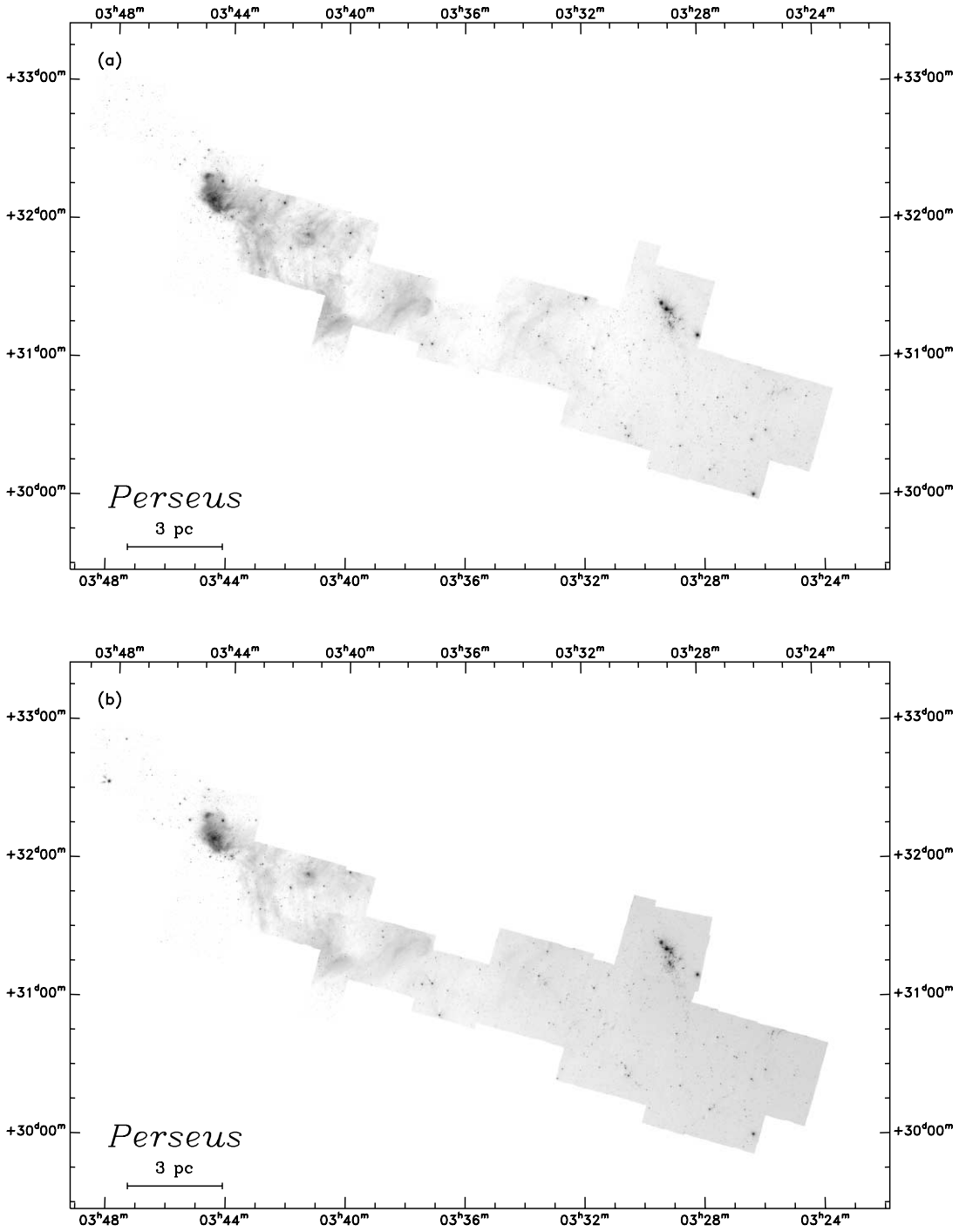

FIG. 4.—Black and white maps of the entire region (shown with a logarithmic stretch) in (*a*) IRAC band 1 (3.6 μm), (*b*) band 2 (4.5 μm), (*c*) band 3 (5.8 μm), and (*d*) band 4 (8.0 μm).

4.2. *Catalogs and Statistics*

In total 123,327 sources were detected by the *Spitzer* observations in at least one IRAC band. Table 2 summarizes the number of sources detected in the Perseus maps with signal-to noise ratios (S/Ns) of at least 7. Sources that have multiple counterparts within the radius used in the band-merging are excluded from this "high-quality" catalog, which we use in the subsequent sections. This corresponds to selecting all sources with detections of quality "A" or "B" in one of the IRAC bands from the delivered c2d catalogs (Evans et al. 2005). Of all the sources in the catalog, the largest fraction is most likely background stars picked up in the most sensitive 3.6 and 4.5 μm bands. This is clearly illustrated in Table 3, where the number of detected sources are split up in the different IRAC bands: with 70,000–110,000 sources detected in IRAC bands 1 and 2 and 10,000–15,000 in band 3 and 4. Of all the reliable detections, about 6700 sources were detected in all four IRAC bands, with about 20% of these not previously detected by 2MASS. Conversely, 65 of the 7933 2MASS sources (0.8%) included in the Perseus mosaic were not detected in any IRAC band. Most of these 65 sources are located at the edge of the *Spitzer* maps, explaining why they are not included in the catalog. Finally, about 541 of the four band detections are found to be extended in one or more bands (classified with "image type" 2 in the

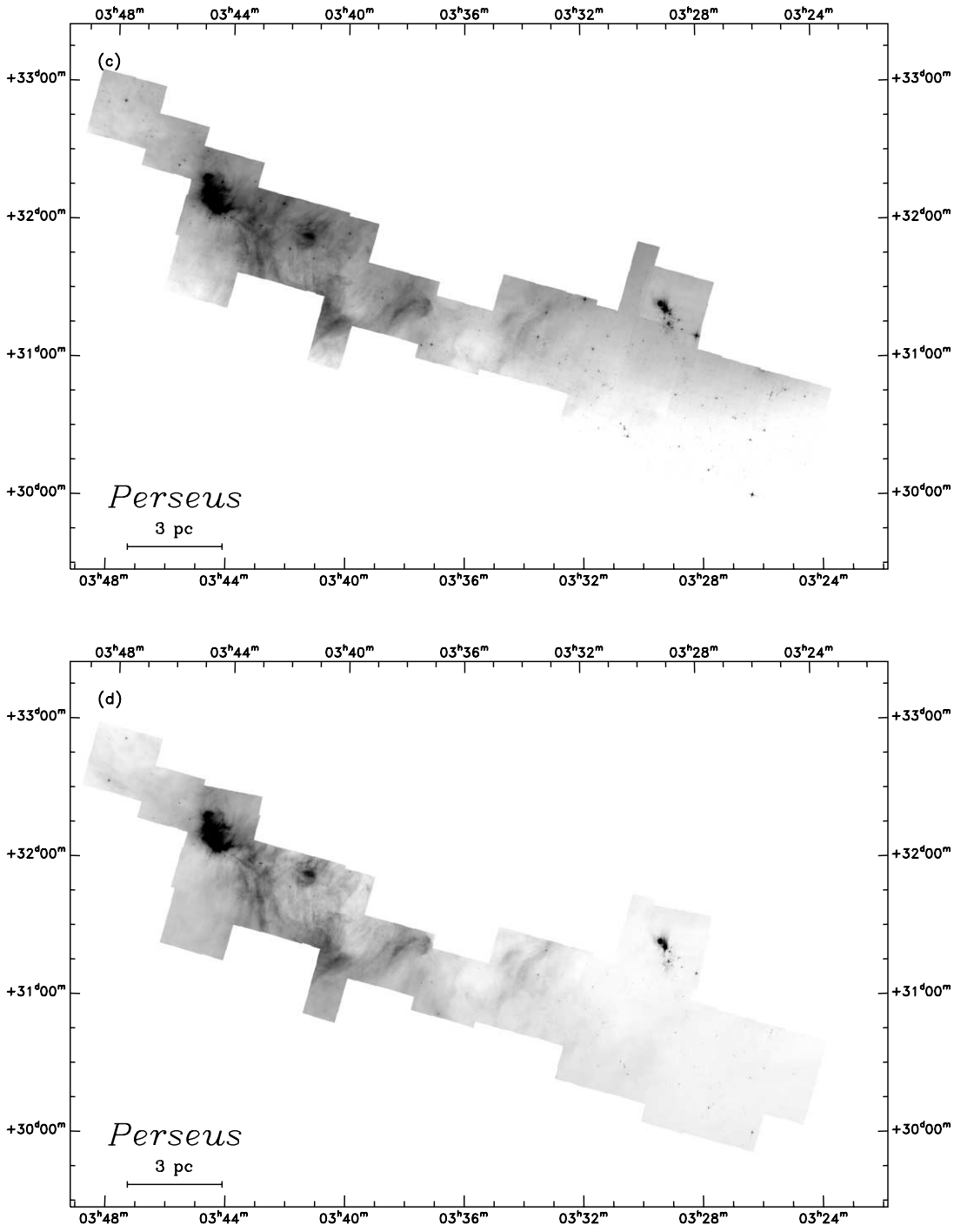

FIG. 4.—*Continued*

c2d catalogs). These are left out of the color-color and color-magnitude diagrams in the following sections, and our high-quality catalog therefore consists of 6192 four-band detections.

Figure 5 shows the differential source counts for the cloud and "off-cloud" areas. The turnover at faint magnitudes illustrates the completeness limit for each IRAC band: 17.5 mag for IRAC1, 16.5 mag for IRAC2, 14.5 mag for IRAC3 and 13.5 mag for IRAC4. An interesting feature is clearly seen in the comparison between the on- and off-cloud fields: the populations in the two agree well in the bright tail of the distribution, but in the faint end there is a clear excess of sources in the off-cloud fields.

Naturally some difference could be expected between the on- and off-cloud fields: the off-cloud fields are selected to have low extinction, whereas most of the on-cloud area has $A_V \gtrsim 2$ mag. Figure 6 compares the differential source counts from a high extinction ($A_V \gtrsim 6$ mag) and a low extinction ($A_V \lesssim 2$ mag) field based on the extinction map in Figure 3. This figure shows that there is an excess of faint sources in the low extinction field, similar to that seen in the off-cloud fields, relative to the counts in the high-extinction fields, i.e., extinction in the cloud shifts the differential source count distribution toward fainter magnitudes.

The double peak seen most clearly in the distribution of IRAC band 1 sources at 17–18 mag in both the on- and off-cloud fields appears to be real. It is not an artifact of the calibration or combination of the different mosaics or frames (e.g., long and short exposures); it is not associated, e.g., with sources only detected

TABLE 2
DETECTION OF SOURCES WITH S/N $\geq$ 7 σ TOWARD PERSEUS

Detection	Number
In at least one IRAC band	123327
In all four IRAC bands	6733
In three IRAC bands	8438
In two IRAC bands	50925
In one IRAC band	57231
In 2MASS only[a]	65
In IRAC only	114975
In four IRAC bands and not 2MASS[a]	1380
Excluding Extended Sources	
Four-band detections	6192
Four-band detections with 2MASS association[a]	5115
Detected in IRAC1+2 and 2MASS[a]	7487

[a] A source is counted as detected in 2MASS if it has a S/N of at least 10 in both H and K_s.

in one epoch; and it is seen across the cloud and not related to any specific region. It therefore seems to reflect either the distribution of stars or background galaxies toward Perseus, but it is not possible to say on the basis of this data set which is more likely. Deep observations and a detailed comparison to a larger sample of fields could possibly shed further light on this issue.

Finally, Figure 7 compares the on-cloud differential source counts to the predicted galactic star counts from the models of Wainscoat et al. (1992) calculated using the C version of the models by J. Carpenter. The model predictions agree well with the observed star counts at bright magnitudes, but they underestimate the source counts at brightnesses fainter than 13–15 mag. The reason is likely contributions from background galaxies, which start to dominate the counts there. For this comparison and our subsequent analysis, the stars are separated from the remaining sources by fitting a (possibly reddened) photosphere (S.-P. Lai et al. 2006, in preparation) to the 2MASS and IRAC measurements. This method relies on 2MASS measurements and does not properly identify fainter stars only picked up in the IRAC bands. It is seen that the observed population of stars agrees well with the predictions of the Wainscoat et al. (1992) models, but also that the background galaxies outnumber the predicted star counts by more than 3:1 at faint magnitudes in some of the bands. This effect is naturally more pronounced for these data than corresponding Serpens data (Harvey et al. 2006) since Perseus is located further from the Galactic plane and the stellar density therefore is lower than in Serpens.

5. THE YSO POPULATION

5.1. *Colors of the Sources*

With more than 6000 sources in the final high-quality catalog detected in all four IRAC bands, it is of great interest to establish general criteria for selecting samples of candidate YSOs. A number of such schemes have been suggested based on IRAC colors alone or in combination with 2MASS or MIPS colors (e.g., Allen et al. 2004; Megeath et al. 2004; Gutermuth et al. 2004; Muzerolle et al. 2004). With the *Spitzer* observations, a high number of photometric data points are obtained that provide strong constraints on the loci in the color-color and color-magnitude planes characterizing YSOs.

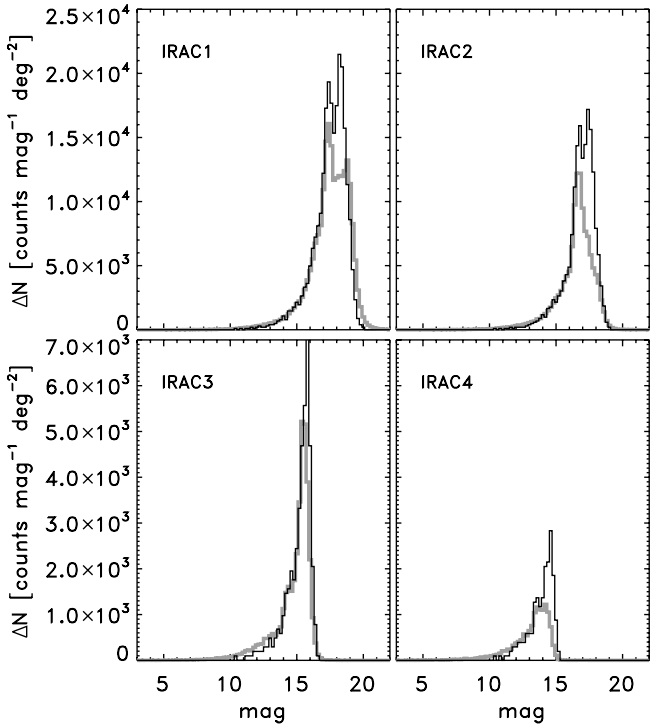

FIG. 5.—Differential source counts for the on- and off-cloud regions (*gray and black lines, respectively*).

A first task is to separate the YSO population from the remainder of the sources toward the cloud, "contaminating the sample," mainly stars and background galaxies. Figures 8–10 show color-magnitude and color-color diagrams for the Perseus cloud compared to the off-cloud and catalogs and data from the SWIRE Elais N1 data set,[10] which is used to estimate the extragalactic component of our catalogs. The SWIRE catalog was processed exactly like the cloud data sets resulting in a catalog consisting of 103557 sources distributed over 6.3 deg^2. For a better comparison to the Perseus data the SWIRE catalog was trimmed down to the same area as covered by the Perseus observations by randomly selecting sources. The SWIRE data also go somewhat deeper due to longer integration time, so the catalog of SWIRE sources was furthermore trimmed to a similar

[10] See J. A. Surace, et al. 2004, VizieR Online Data Catalog, 2255, 0.

TABLE 3
DETECTION OF SOURCES TOWARD PERSEUS (PER BAND)

Detections	3.6 μm	4.5 μm	5.8 μm	8.0 μm
With S/N of at least 7	110585	76425	14999	9318
With S/N of at least 10	85913	60042	10189	7010
With S/N of at least 15	53592	34619	6644	4810
With final sample (excluding extended sources)	104341	74877	14832	8997
With 2MASS associations (S/N at least 10 in H and K_s)	7532	7778	7206	5434

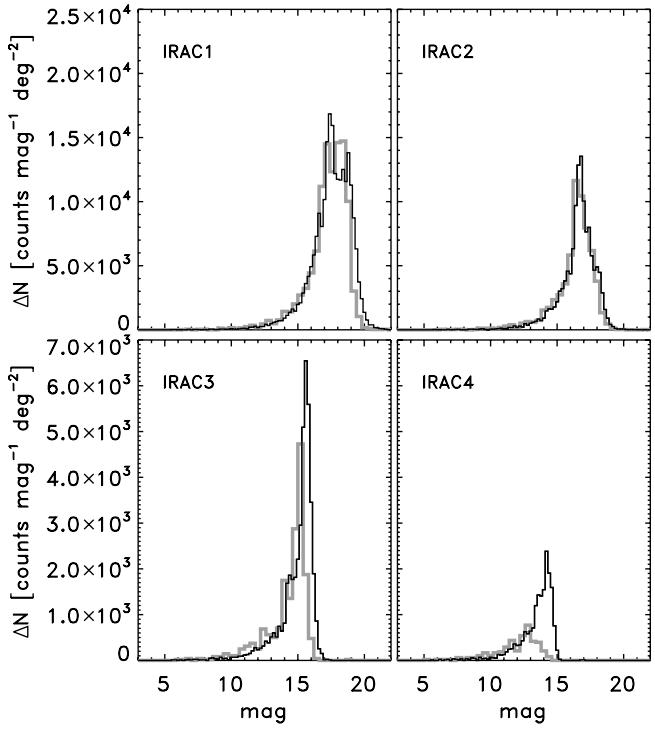

FIG. 6.—Differential source counts for a low- and high-extinction fields (*black and gray lines, respectively*).

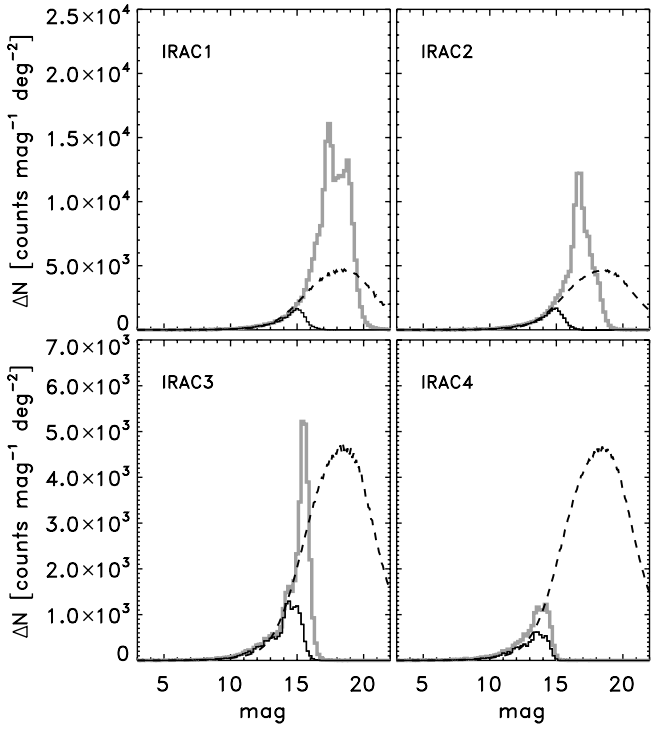

FIG. 7.—Differential source counts for all on-cloud sources as in Fig. 5 (*gray lines*) and objects that can be classified as stars through fits to their 2MASS and IRAC measurements by a (reddened) photosphere (*black lines*). Also shown are the predictions for the star counts from the models of Wainscoat et al. (1992) (*dashed lines*). An excess of background galaxies is clearly seen at faint magnitudes from the comparison between the distribution of stars from the model predictions and the actual number counts. Note that the fainter stars in the *Spitzer* observations are not classified as such due to lack of 2MASS data. The difference between the black solid lines and the dashed lines at faint magnitudes therefore reflects the completeness of the 2MASS data rather than an actual discrepancy between the IRAC observations and the model predictions.

completeness limit as the Perseus data. In the analysis only sources with high-quality detections (as described in § 4.2) have been included. In each of the diagrams the group of stars constitute a distinct group centered around zero colors. Comparing the [8.0] versus [4.5] − [8.0] color-magnitude diagram for the Perseus on-cloud region to the off-cloud regions and SWIRE data there obviously is a significant excess of sources with [4.5] − [8.0] > 0.5 and [8.0] magnitudes brighter than 14 − ([4.5] − [8.0]) as indicated by the dashed lines in the top right panel. In total, 400 such objects are found that as a first cut represent the candidate YSOs toward Perseus. In the "on-cloud" and, in particular, the SWIRE diagrams a large population of fainter red objects is seen, which are likely dominated by background galaxies. At faint magnitudes the diagram becomes inadequate for separating these three basic group of objects and it becomes necessary to look at the full photometric data for classification. In particular, stars are separated from the remaining objects by fitting a (possibly reddened) photosphere (S.-P. Lai et al. 2006, in preparation) as described above.

Some sources do not show an excess in the IRAC bands but do show an excess in the MIPS 24 μm observations (discussed by L. Rebull et al. 2006, in preparation). The combination of the long-wavelength IRAC and MIPS observations is expected to be particularly sensitive to infrared excesses since photospheric colors are expected to be zero and have previously been applied to the selection of YSOs (Muzerolle et al. 2004). As above, sources with excesses in the MIPS band can be selected from [24] − [8] > 0.7 and [24] < 12 − ([24] − [8.0]). This selection adds another 37 candidate YSOs to our catalogs. These include objects with faint excesses only detectable at longer wavelengths (i.e., more evolved "Class III" objects). Embedded YSOs, with some degree of PAH emission contributing to the IRAC band 4 emission (shifting them rightward in Fig. 8 to the faint side of the magnitude cutoff) or with certain geometries of their circumstellar envelopes, can also fall into this category, however. Still, this is a small fraction (≈9%) compared to our total list of 400 YSO candidates, but it illustrates how the inclusion of even longer wavelength data adds to the information about the sample of YSOs.

A small fraction, 3%–4%, of the nonstellar objects in the SWIRE and off-cloud diagrams are bright enough at 8 or 24 μm to be misclassified as YSOs. If the same fraction applies to the Perseus diagram, about 24 (≈6%) of the YSOs in the on-cloud region might in fact be extragalactic objects. This number is an upper limit, though: any extragalactic object will be behind the cloud, extincted, and thus moved in the direction of the extinction vector toward the faint side of the magnitude cutoff (*nonvertical dashed line*) in the [8.0] versus [4.5] − [8.0] diagram in Figure 8.

Figures 9 and 10 show the location of the different groups of sources in two other diagrams that have been used for classifying YSOs from samples of *Spitzer* sources, the [3.6] − [4.5] versus [5.8] − [8.0] (Megeath et al. 2004) and $H - K_s$ versus K_s − [4.5] (Gutermuth et al. 2004) color-color diagrams. The locations of the YSO candidates agree well with the predicted locations in these two diagrams: in the [3.6] − [4.5] versus [5.8] − [8.0] diagram, the YSOs are expected to fall in a group with colors around ([3.6] − [4.5], [5.8] − [8.0]) = (0.7, 0.5) or redder according to Allen et al. (2004) and Megeath et al. (2004). It is also clear, however, that this diagram in itself is not sufficient to separate the YSO candidates from, in particular, the background galaxy populations. In contrast, the $H - K_s$ versus K_s − [4.5] diagram appears to be better suited for selecting YSO candidates. The detected galaxies and stars are largely overlapping with colors close to zero (compare, e.g., to the SWIRE diagram) whereas the YSO candidates

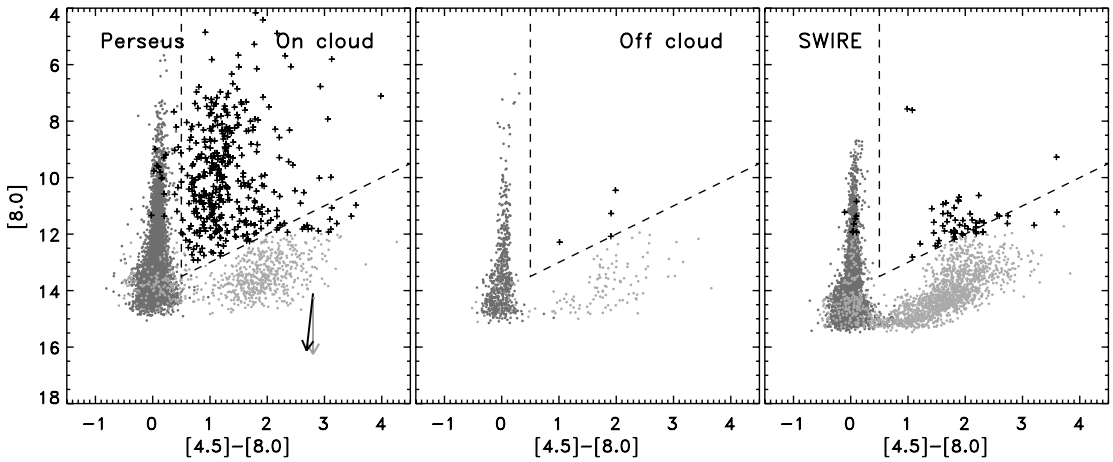

FIG. 8.—[8.0] vs. [4.5] − [8.0] color-magnitude diagrams based on the high-quality catalogs (see text) with the Perseus "on-cloud" regions (*left*), "off-cloud" region (*middle*), and trimmed SWIRE catalog (*right*). In each panel stars have been indicated by dark-gray dots, YSO candidates by black plus signs, and other sources by light-gray dots. The distinction between YSO candidates and other sources was mad predominantly on the basis of this diagram, with YSO candidates taken from the top right part of the diagram above and right of the two dashed lines with a few additional sources added based on their [8.0] − [24] colors (see discussion in text). Two extinction vectors are shown corresponding to $A_K = 5$ mag. The gray vector was derived for diffuse ISM regions by Indebetouw et al. (2005). The black vector, appropriate for the dense regions found in molecular clouds and cores, was derived from deep near-infrared and *Spitzer* observations of dense cores (T. Huard et al. 2006, in preparation).

have redder $H - [4.5]$ colors, in particular. The drawback to this diagram is the requirement that the YSOs are all detected at H and K_s. It turns out that only 280 (70%) of the YSO candidates have 2MASS associations, i.e., 10 σ detections in both H and K_s (305 or 76% of the YSO candidates are associated with 2MASS sources with 5 σ detections in H and K_s). The sources not detected by 2MASS are likely more deeply embedded sources or brown dwarfs, and therefore the selection of YSO candidates using 2MASS criteria is somewhat biased against such objects. One could, on the other hand, suspect that the $H - K_s$ versus $K_s - [4.5]$ diagram would identify sources not included in the other diagrams, given that only detections in IRAC bands 1 and 2 are required. This, however, seems not to be the case as only a few "other" sources are identified in the red part of the diagram, as also shown by the comparison to the off-cloud diagram. The best way to separate faint YSOs from galaxies seems to be with much deeper *JHK* data.

5.2. *Classification of YSO Candidates*

With a sample of candidate YSOs selected, a next natural step is to search for trends in evolution between these. The most used classification scheme for YSOs is based on their spectral slope, $\alpha = (d \log \lambda F_\lambda / d \log \lambda)$ (Lada 1987), dividing the YSOs into Class I, II, and III with increasingly blue SEDs. This classification scheme is thought to represent (roughly) the evolution of YSOs from their embedded protostellar phases through their pre–main-sequence stages. The Lada classification scheme has subsequently been expanded with a group of "flat-spectrum" YSOs suggested to represent a transitional phase between the Class I and II stages (André & Montmerle 1994; Greene et al. 1994). Earlier in the evolution of low-mass protostars, the so-called Class 0 objects (André et al. 1993), are thought to represent the most deeply embedded YSOs. This class of objects is defined by the SEDs at submillimeter wavelengths, where they emit more than 0.5% of their total bolometric luminosity at wavelengths longer than 350 μm, and not by their mid-infrared signatures: previously these objects were in general not detected at mid-infrared wavelengths. A number of Class 0 objects are known in Perseus, and we return to these in § 6. In the remainder of this section, however, we do not distinguish these deeply embedded protostars from the Class I objects.

For each of the sources in the Perseus YSO catalog, a spectral index is assigned on the basis of its photometry from 2MASS K_s

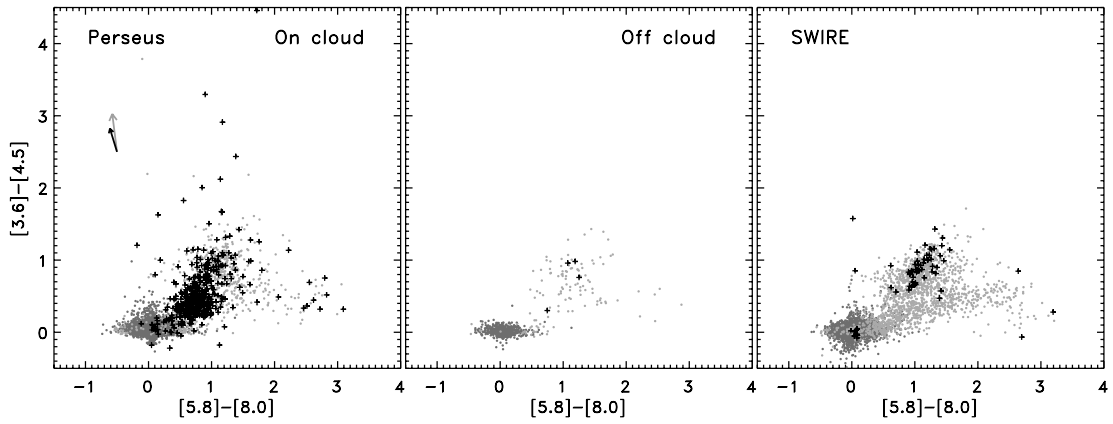

FIG. 9.—[3.6] − [4.5] vs. [5.8] − [8.0] color-color diagram for the "on-cloud" (*left*), "off-cloud" (*middle*), and SWIRE (*right*) fields. Sources, symbols, and extinction vectors are as in Fig. 8.

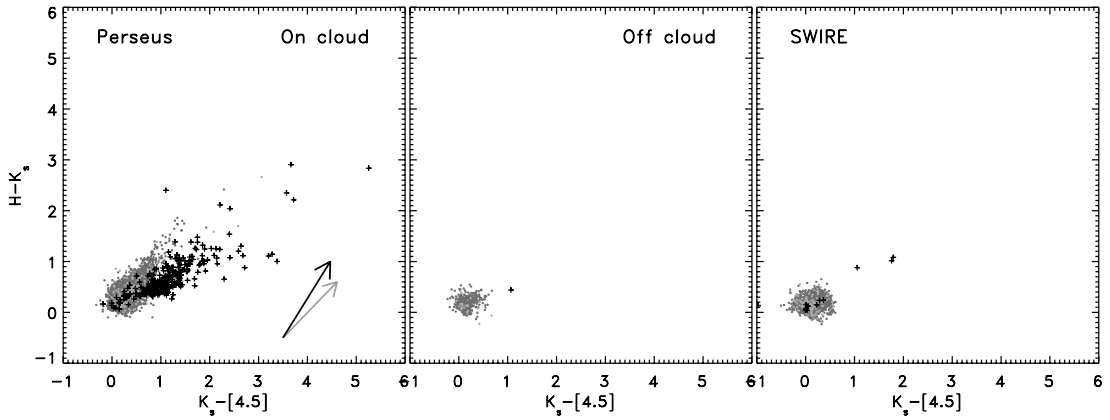

FIG. 10.—Same as in Figs. 8 and 9, but for an $H - K_s$ vs. $K_s - [4.5]$ color-color diagram. All sources with high-quality detections in the IRAC bands 1 and 2 (see text) and 10 σ detections in H and K_s included. Otherwise, sources and symbols are as in Figs. 8 and 9; extinction vectors shown are for $A_K = 2$ mag.

through MIPS 24 μm. Figure 11 plots the sources with different spectral indexes in the $[3.6] - [4.5]$ versus $[5.8] - [8.0]$ diagrams, following the division by Greene et al. (1994), in which Class I objects have $\alpha \geq 0.3$, "flat-spectrum" objects have $-0.3 \leq \alpha < 0.3$, Class II objects have $-1.6 \leq \alpha < -0.3$, and Class III objects have $\alpha < -1.6$. With this scheme, 243 of the YSOs in Perseus are classified as Class II, 71 as "flat-spectrum" and 54 as Class I YSOs.

Based on a theoretical study, Allen et al. (2004) suggested that the Class II objects, i.e., pre–main-sequence stars with disks, would have colors $0.0 < [3.6] - [4.5] < 0.8$ and $0.4 < [5.8] - [8.0] < 1.1$, whereas the Class I objects, i.e., objects still embedded in a circumstellar envelope, would have colors $[3.6] - [4.5] > 0.8$ and/or $[5.8] - [8.0] > 1.1$. This division between Class I and II objects is seen to be in good agreement with the α classification described above for 219 (90%) of the Class II and 50 (93%) of the Class I objects. Fourty-two (59%) of the "flat-spectrum" sources fall in the region of Class I objects in the scheme of Allen et al. (2004), and 28 (39%) in the region of Class II objects, underscoring that this group lies between the Class I and II objects. It may not be that surprising that these trends are found, given that the estimate of α and the color diagrams are essentially based on the same measurements. The classification is also not unambiguous: Class II objects with edge-on disks for example have colors similar to the Class I objects.

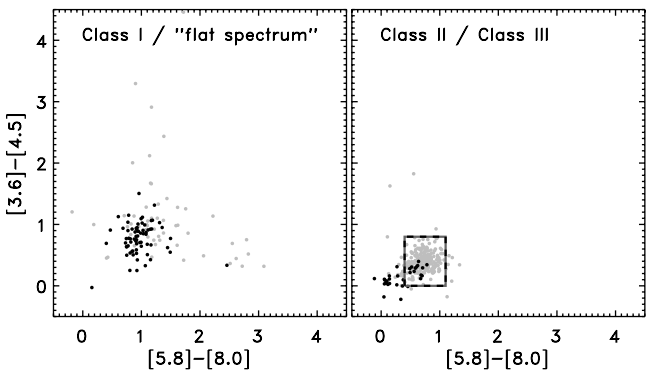

FIG. 11.—$[3.6] - [4.5]$ vs. $[5.8] - [8.0]$ color-color diagrams for the YSO sample. The symbols are colored according to their classification based on their spectral slope α [$\alpha = (d \log \lambda F_\lambda / d \log \lambda)$] in the scheme of Lada (1987): Class I objects ($\alpha \geq 0.3$) and "flat-spectrum" ($-0.3 \leq \alpha < 0.3$) sources are shown in the left panel with gray and black symbols, respectively. Likewise, Class II ($-1.6 \leq \alpha < -0.3$) and Class III objects ($\alpha < -1.6$) are shown in the right panels with gray and black symbols, respectively. The box delineating Class II objects from Allen et al. (2004) has furthermore been indicated in the right panel (*black and gray dashed rectangle*).

A cross-check with the SIMBAD astronomical database reveals that 217 (or 54%) of the YSO candidates from the list in this paper are associated with known objects—almost all YSO-like—within a search radius of 5″. Expanding the search radius to 10″ only increases this number slightly to 228. Interestingly, only 35% and 39% of the Class I and "flat-spectrum" sources are associated with known sources, whereas the numbers for the Class II and III objects are 60% and 72%, respectively. It therefore appears that the new YSO candidates in our catalog are predominantly faint, embedded sources with significant mid-infrared excesses, as should be expected from the high sensitivity of *Spitzer* compared to previous surveys included in SIMBAD—in particular those based on *IRAS* data.

Our selection of YSO candidates does not properly identify Class III objects: of our YSO candidates, 32 objects have $\alpha < -1.6$ consistent with Class III objects (16 of these 32 are selected as YSO candidates on basis of the criterion involving their IRAC4 and MIPS 24 μm colors, a high fraction compared to the only $\approx$9% of the entire YSO population selected in this way). Given that the emission from such objects is largely photospheric and therefore difficult to distinguish from stars, this sample is not complete. Additional data from other wavelengths are necessary for addressing these issues and properly cross-identifying YSOs (S.-P. Lai et al., 2006, in preparation). One of the goals for c2d is to include such data—also to refine the classification schemes and thus our understanding of the evolution of YSOs.

5.3. *Spatial Distribution of YSOs*

Figure 12 shows the identified Class I and II YSO candidates plotted over the 4.5 μm IRAC image. The two clusters around NGC 1333 and IC 348 clearly stand out with a high density of sources. Figure 13 shows the color-color and color-magnitude diagrams for the extended cloud (excluding the clusters) compared to each of these two clusters. The NGC 1333 region was defined as ranging from $03^h28^m00^s$ to $03^h30^m00^s$ in right ascension and $+31^\circ06'00''$ to $+31^\circ30'00''$ in declination, while the IC 348 region was defined as ranging from $03^h43^m12^s$ to $03^h46^m00^s$ in right ascension and $+31^\circ48'00''$ to $+32^\circ24'00''$ in declination (all J2000.0), including the areas studied in the GTO programs. The numbers of total YSO candidates and numbers of Class I and II objects in each of these regions are summarized in Table 4. Significant differences exist between IC 348,

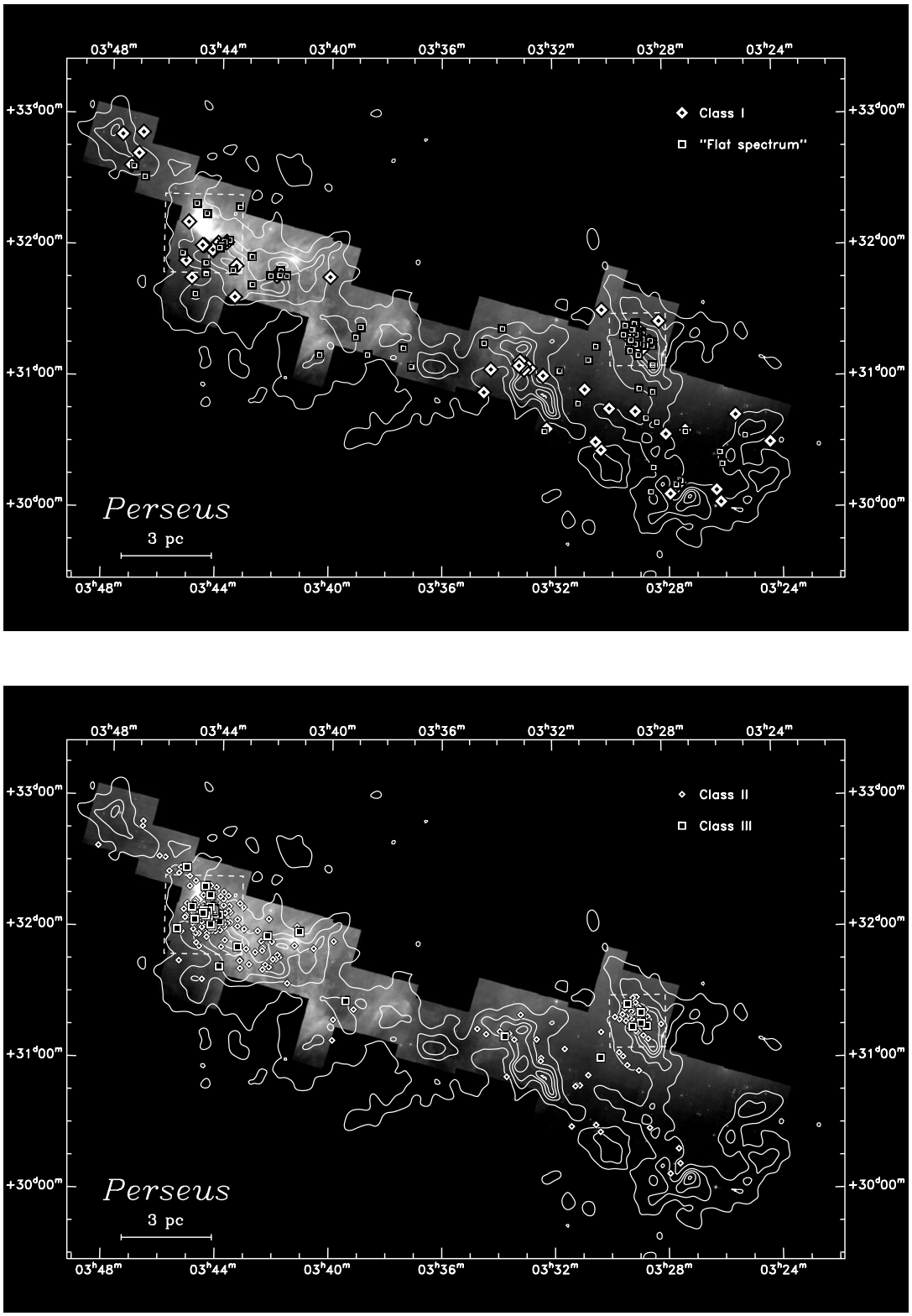

FIG. 12.—Distribution of Class I objects (*top*) and Class II objects (*bottom*) plotted on top on a 4.5 μm image of Perseus with an extinction map overlay (see also Fig. 3). The adopted boundaries for IC 348 and NGC 1333 have been indicated by the dashed lines.

NGC 1333, and the remaining cloud. The two clusters contain similar numbers of YSO candidates and contain about half of the total YSO candidates in the surveyed area. The spatial density of YSO candidates is 5–6 times higher in each of the clusters compared to the extended cloud. In the extended cloud most of the YSOs appear to be following the extinction with concentrations of predominantly Class I objects around B1, B5, L1448 and L1455, and an additional number of Class II objects about 40′ southwest of the main concentration of sources in IC 348. Cambrésy et al. (2006) recently suggested the existence of a cluster separate from the main IC 348 cluster at this location through maps of the spatial density of sources derived from 2MASS data. This cluster

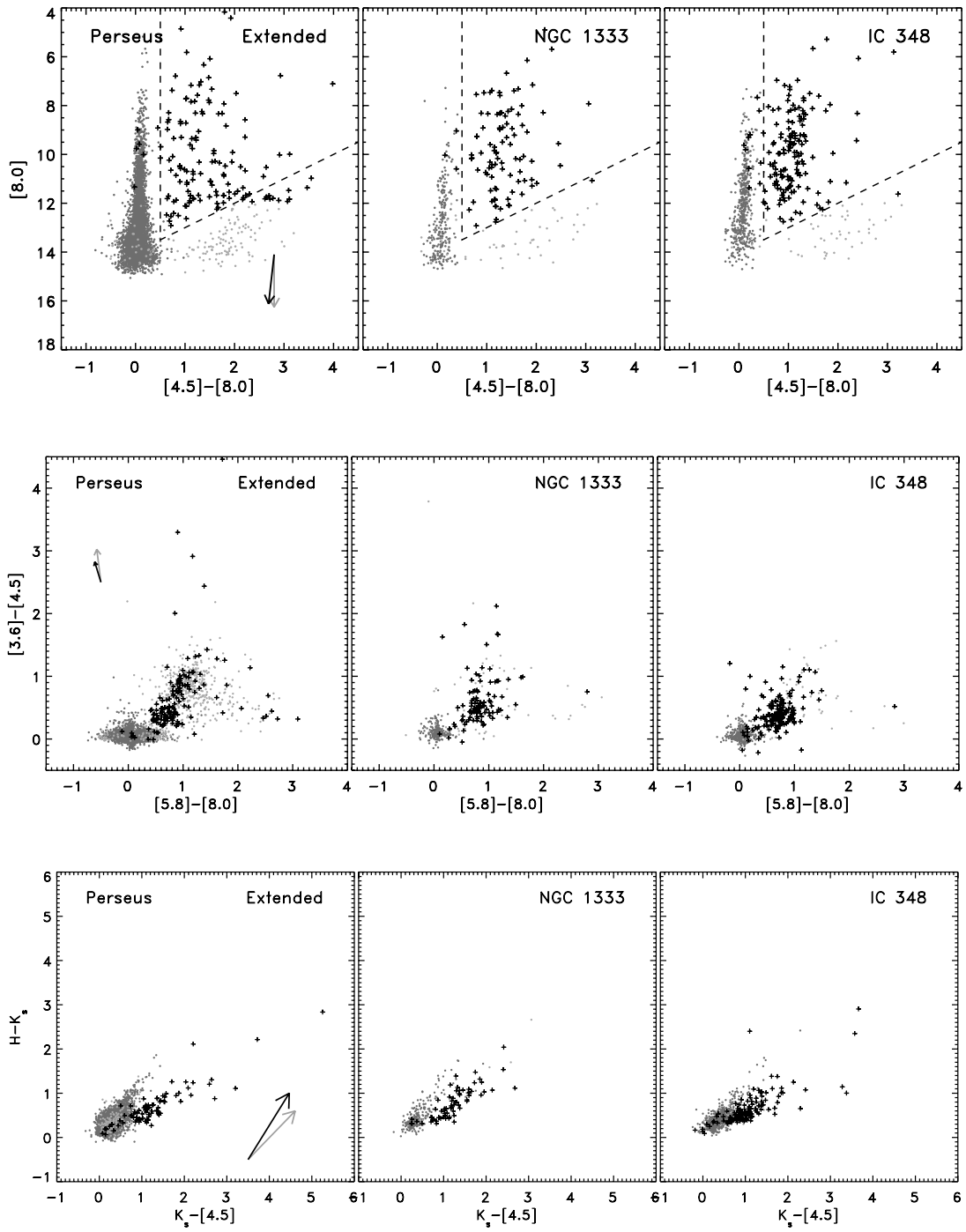

FIG. 13.—Color-color and color-magnitude diagrams from the extended cloud excluding NGC 1333 and IC 348 (*left*), NGC 1333 only (*middle*), and IC 348 only (*right*). As in Figs. 8–10, stars have been indicated by dark gray dots, YSO candidates by black plus signs, and other sources by light-gray dots.

is not included in the statistics for IC 348 below but rather together with the remaining cloud.

Table 4 also shows that there is a significant difference in the relative numbers of Class I/"flat-spectrum" and Class II objects among the two clusters and the extended cloud, with the more embedded Class I objects being more numerous in NGC 1333 than in IC 348, whose YSO population predominantly consists of Class II YSOs. A difference between the two clusters is consistent with near-infrared studies suggesting an age of about 2 Myr for IC 348 (Luhman et al. 2003) and <1 Myr for NGC 1333 (Lada et al. 1996; Wilking et al. 2004). The relative number of Class I and "flat-spectrum" objects compared to the overall YSO candidates is significantly higher in the extended cloud compared to these two clusters, however, suggesting that a significant fraction of the recent and current star formation in Perseus is going on in the extended cloud, including the smaller groups surrounding B1, L1455, and L1448. In fact, 61% of the Class I YSOs toward Perseus are located outside the two main clusters, compared to only 28% of the Class II YSOs. Even within the group of Class I and "flat-spectrum" sources it seems that the extended cloud contains more of the red Class I objects compared to the numbers in NGC 1333. A more detailed study of the clustering properties of the different groups of YSOs in these regions—and comparison to other similar selections of YSOs in other cloud

TABLE 4
NUMBER OF YSO CANDIDATES IN IC 348 AND NGC 1333 COMPARED TO THE REMAINING CLOUD

Parameter	Total Surveyed Area	IC 348	NGC 1333	Remaining Cloud
Area (deg^2)	3.86	0.36	0.17	3.33
YSO candidates	400	158	98	144
YSOs per square degree	103.6	438.9	576.5	43.2
Class I	54 (14%)	11 (7%)	10 (10%)	33 (23%)
"Flat spectrum"	71 (18%)	11 (7%)	25 (26%)	35 (24%)
Class II	243 (61%)	116 (73%)	58 (59%)	69 (48%)
Class III	32 (8%)	20 (13%)	5 (5%)	7 (5%)

NOTE.—Numbers in parentheses indicate the relative fraction of YSOs of different classes compared to the total number of YSOs in the specific regions.

regions—could shed further light on differences in YSOs formed in large clusters compared to objects formed in small groups or in relative isolation.

6. DEEPLY EMBEDDED PROTOSTARS AND ASSOCIATED OUTFLOWS

Perhaps the most spectacular features in the maps are the prominent outflows clearly seen in bands 2 and 3, where molecular hydrogen emission from shocked gas dominates. Figure 14 shows band 2 images of a selection of the outflows outside the two main clusters in Perseus. Since the outflow activity is thought to be related to the accretion onto the central star/disk system, it has been suggested that sources with such strong outflow activity represented the earliest, most deeply embedded stages of low-mass protostellar evolution (Bontemps et al. 1996), the Class 0 stage (André et al. 1993). On the other hand, the exact same outflows pose a problem for the source catalogs above. The deeply embedded protostars driving these outflows likely show extended emission at 4.5 and 5.8 μm from which it may be problematic to extract the embedded sources.

6.1. *L1448*

Figure 14a shows the outflows in the L1448 region with known embedded protostars overplotted. The L1448-C source is one of the best studied Class 0 protostars at a range of wavelengths and is known to drive a parsec scale outflow in the north-south direction. This outflow is clearly identified in our maps extending to the north, where the outflow emission makes a break at the positions of another known Class 0 protostar, L1448-N (or L1448-IRS3). L1448-N is a binary with a separation of about 7″ (e.g., Looney et al. 2000). Two sources are seen at the position of L1448-N(A) and L1448-N(B) with the eastern one, L1448-N(A), corresponding to the brighter source in the IRAC maps with the exception of band 1 (Fig. 15). Interestingly the western source, L1448-N(B), is the stronger of the two in 2.7 mm observations by Looney et al. (2000). The *Spitzer* maps also show some indication of two fan-shaped outflows emerging from the central source in the north direction, and separating the point-source fluxes is subject to significant uncertainties. Only faint extended emission is seen at the location of a third source, L1448-NW (L1448-IRS3C), northwest of the L1448-N(A) and L1448-N(B). Almost parallel to the L1448-C outflow, about 8′ to the west, the outflow from the Class 0 source L1448-IRS2 (O'Linger et al. 1999) is seen. Another outflow is observed close to L1448-IRS2 in the northwest direction. This outflow is associated with the L1448-IRS1 source, which is located outside our mosaic in IRAC bands 2 and 4 but clearly identified in bands 1 and 3. The outflows from L1448 are likely extending even further south: between L1455 and L1448 two prominent knots associated with shocked gas are identified at ($03^h25^m51^s$, $+30°35'13''$) and ($03^h26^m04^s$, $+30°39'02''$), the latter is associated with HH 277, and further south at the position of HH 278 ($03^h26^m59^s$, $+30°25'58''$) pointing back toward the L1448 region. Shocks are seen on similar scales pointing back toward the NGC 1333 region in our maps around the position of HH 746 at ($03^h28^m32^s$, $+30°52'10''$).

Toward L1448-C, two sources are clearly seen in the IRAC images separated by about 8″ (Fig. 15), which we refer to as L1448-C(N) (at the position of the millimeter source L1448-mm) and L1448-C(S). Of these only one source is identified in all four IRAC bands in our source extraction. The source recognized from millimeter interferometric observations as the driving source of the outflow—and which is detected in the millimeter continuum interferometric measurements—is only detected in IRAC band 3 and MIPS 24 μm by the source extraction software, even though it is clearly identified as a separate point source. The reason is likely the confusion with the extended emission from the outflows in the other bands. We extract a flux for this source from aperture photometry in a 2 pixel radius (2.″4) aperture with a sky annulus extending from 2 to 6 pixels (2.″4–7″) using the `aper` procedure from the IDL Astronomy User's library. L1448-IRS2 also does not make it to the high-quality catalog; it shows extended emission in IRAC2 and IRAC3 and is therefore not included in our high-quality catalog used in the color-color and color-magnitude diagrams above. The source extractor does identify this source and it is included in the overall catalog of sources from c2d.

6.2. *L1455*

The outflows in L1455 pose an interesting puzzle. Previously three YSOs had been identified in this region (Juan et al. 1993): L1455-IRS1 (IRAS 03245+3002), L1455-IRS2 (IRAS 03247+3001), and L1455-IRS3 (IRAS 03249+2957). L1455-IRS2 is driving a north-south outflow and associated with the red nebular object, RNO 15. An outflow is stretching roughly northwest-southeast in CO observations (Goldsmith et al. 1984) and is likely associated with a number of Herbig-Haro objects (Bally et al. 1997). The driving source of this outflow is not clear: Juan et al. (1993) suggested that L1455-IRS1 was the driving source of the entire complex CO outflow observed by Goldsmith et al. (1984), but Bally et al. (1997) argued that two separate outflows had to be responsible for the northwest-southeast outflow and an outflow extending in the east-west direction (also responsible for HH 317). Indeed, Davis et al. (1997) showed from CO 3–2 observations that L1455-IRS1 was associated with an outflow in the northeast-southwest direction and likely responsible for HH 318.

In the IRAC2 image the northwest-southeast outflow is clearly identified together with a number of the Herbig-Haro objects

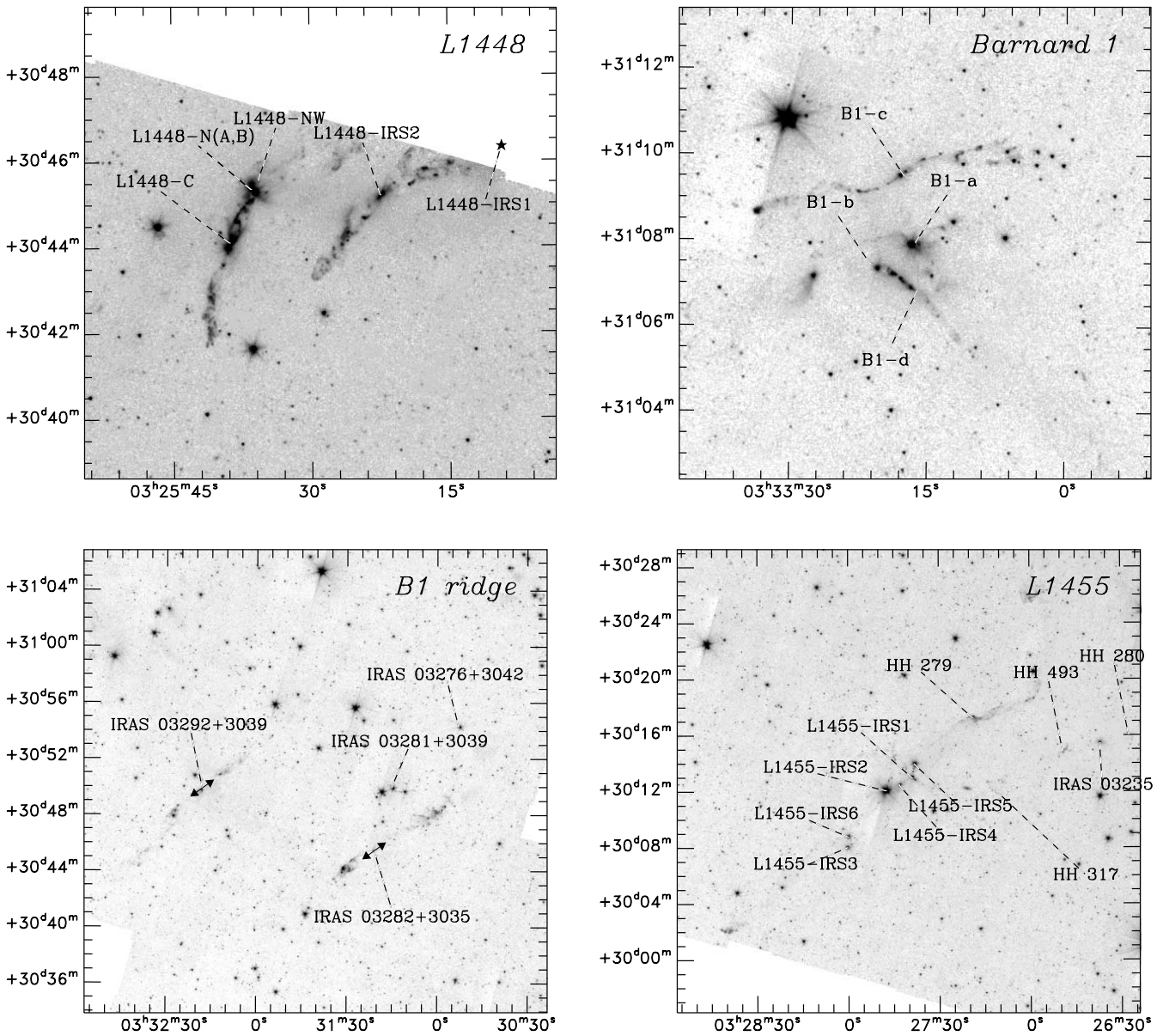

FIG. 14.—Images of outflows in Perseus in band 2. *Top panels:* L1448 (*left*) and B1 (*right*). *Bottom panels:* B1 ridge (*left*) and L1455 (*right*). In the L1448 panel the location of L1448-IRS1 (seen in the band 1 and band 3 images) is indicated with a black star. In the B1 ridge panel the directions of the outflows from IRAS 03292−3039 and IRAS 03282−3035 are indicated by black arrows. Similar arrows are shown for L1455-IRS1 and L1455-IRS4 in Fig. 16, where the location of HH 318 is also indicated.

observed by Bally et al.: HH 279 ($03^h27^m19^s$, $+30°17'16''$), HH 317 ($03^h27^m11^s$, $+30°11'59''$), and HH 318 ($03^h27^m44.^s6$, $+30°14'17''$). In addition, a nebulosity is seen south of HH 279 delineating the southern part of the blueshifted lobe of the CO outflow. About 15′ southwest of the central L1455 cluster another nebulosity is seen, which could represent the other lobe of the northwest-southeast outflow. Two additional infrared sources are observed close to L1455-IRS1 and L1455-IRS2: one in between the two sources, which we name L1455-IRS4,[11] and one slightly northwest of L1455-IRS1, which we name L1455-IRS5. The close proximity of these sources suggests an interaction, which may have caused the precession of the northeast-southwest outflow, as discussed by Davis et al. (1997). Of the four sources, L1455-IRS2 is clearly the strongest at mid-infrared wavelengths, followed by L1455-IRS5. On the other hand, L1455-IRS1 and L1455-IRS4 are associated with the strongest dust continuum peaks in maps of the (sub)millimeter emission, as shown in a map at 350 μm taken with the SHARC II bolometer array at the Caltech Submillimeter Observatory (Fig. 16; J. Wu et al. 2006, in preparation; see also Hatchell et al. 2005; Enoch et al. 2006). From the color criteria discussed above, L1455-IRS1 and L1455-IRS4 would both fall in the Class I group, whereas L1455-IRS2 and L1455-IRS5 would be more evolved Class II objects. It is therefore also likely that L1455-IRS1 and L1455-IRS4 are responsible for the northeast-southwest and southwest-northeast outflows, respectively, and their association with the dust continuum peaks furthermore suggests their deeply embedded natures. L1455-IRS3 is likewise classified as a Class I source, but no continuum peak is seen toward this source in the SCUBA maps of Hatchell et al. (2005; unfortunately it falls just outside the field observed by Enoch et al. 2006). A companion, L1455-IRS6, is seen 40″ north of L1455-IRS3 with

[11] Note that Froebrich (2005) erroneously identified a source close to this position with the RNO 15 nebula.

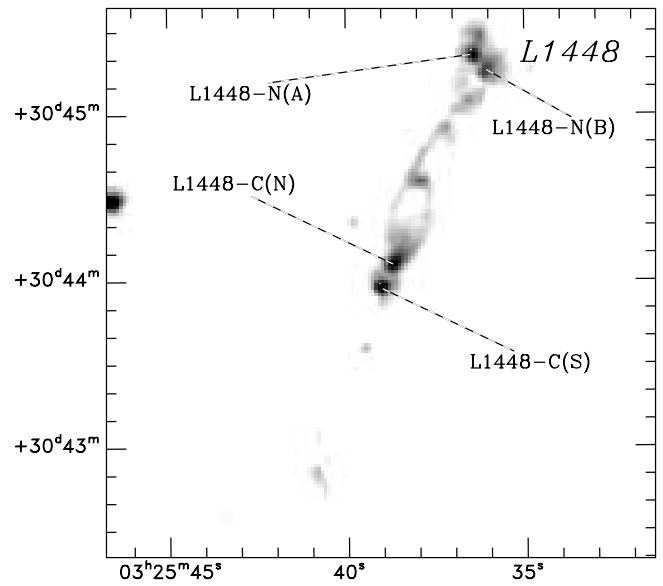

FIG. 15.—Zoom-in on the IRAC2 image around L1448-C and L1448-N (note that the scaling of the image is slightly different from Fig. 14). The separation of L1448-N into L1448-N(A) and L1448-N(B) and L1448-C into L1448-C(S) and L1448-C(N) is clearly seen.

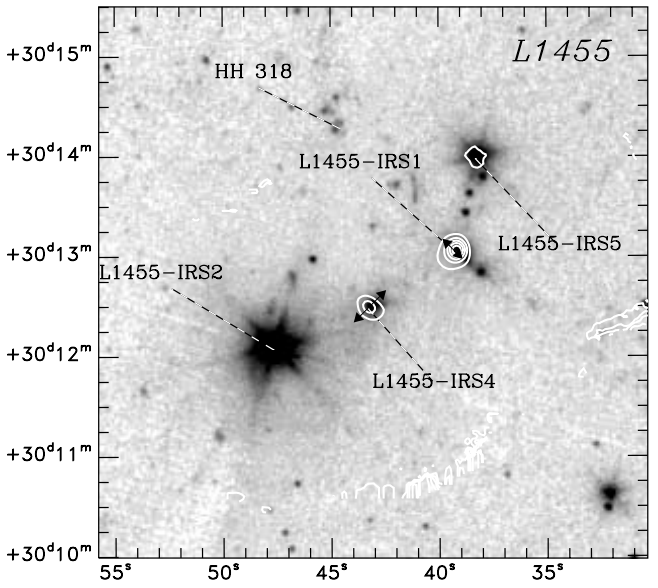

FIG. 16.—Zoom-in on the IRAC2 image of the central region of L1455 from Fig. 14. Overlaid in white contours are a 350 μm continuum image from the SHARC II bolometer array at the Caltech Submillimeter Observatory (J. Wu 2006, in preparation). The contours are plotted at 15%, 30%, 45%, ... of the peak flux (at the position of L1455-IRS1). The approximate directions of the outflows from L1455-IRS1 and L1455-IRS4 are indicated by black arrows.

an SED typical of a Class II source. Of the two candidate embedded protostars, L1455-IRS1 and L1455-IRS4, L1455-IRS1 has full photometry in our high-quality catalog from 3.6 to 24 μm, whereas L1455-IRS4 only is recognized at the two longer wavelengths.

Finally, two knots are seen at ($03^h26^m27^s$, $+30°16'01''$) and ($03^h26^m49^s$, $+30°14'54''$) in the IRAC2 maps associated with HH 280 and HH 493 distributed symmetrically on a east-southeast to west-northwest axis through IRAS 03235+3004, which Walawender et al. (2004) suggested was the driving source of this outflow. IRAS 03235+3004 is detected as a candidate Class I object in our catalogs and is associated with a strong continuum peak in the maps of Hatchell et al. (2005) and Enoch et al. (2006).

6.3. *B1 and Beyond*

Finally, we would like draw the attention to the outflow activity around the B1 region, which has recently received much attention as one of the very active regions of star formation in the Perseus complex with a number of submillimeter clumps with embedded protostars and Herbig-Haro objects (Hirano et al. 1999; Matthews & Wilson 2002; Walawender et al. 2005). A number of these prominent outflows are observed in the IRAC data. The most striking is the precessing outflow clearly associated with the B1-c source. This source stands out very clearly in the RGB image (Fig. 2), with a very red color, suggesting the embedded nature of this object. Of the other sources in this region, B1-a shows extended emission that dominates the source at 3.6 μm. The source is therefore not included in the high-quality catalog used for the color-magnitude diagrams above.

The B1-b and B1-d submillimeter cores suggest an interesting interaction: toward the B1-b position a point source with colors consistent with an embedded YSO is clearly seen with a jet extending southwest of the core toward the position of the other submillimeter core, B1-d. On the other side of this core the jet seems to be making a break and thereafter extends further south with weaker emission. The break occurs at the exact position of the B1-d submillimeter core suggesting some interaction between the outflows and the core. An outflow extending from a source embedded in the B1-d core can of course also not be ruled out: no point source is seen in the IRAC bands, but a faint MIPS source is seen toward the position of the submillimeter core. Previously no outflow had been associated with the B1-b sources, but this may have been due to the confusion in the region. Based on maps of the dust continuum emission from SCUBA and 3 mm interferometric measurements from the Nobeyama Millimeter Array, B1-b was found to be a binary by Hirano et al. (1999) with a separation of $\approx 20''$, but it does not show up as two separate sources in the *Spitzer* images.

In addition to these sources, the emission-line star, LkHα 327, is clearly the strongest source in the IRAC bands located northwest of the submillimeter cores. LkHα 327 is identified as a Class II object by our criteria. Four additional candidate Class I YSOs are identified southwest of the main concentration of submillimeter cores. These sources are weak compared to the sources associated with the central cores, but might be associated with faint dust continuum emission.

The region southwest of the main B1 core, the B1 ridge, is also interesting with two strong outflows associated with the two *IRAS* sources, IRAS 03282+3035 and IRAS 03292+3039. Both of these sources are associated with peaks in dust continuum emission in the maps of Hatchell et al. (2005) and Enoch et al. (2006), but neither is picked up in the high-quality catalog above. A weak IRAC source is associated with IRAS 03282+3035, which is somewhat extended in a number of the IRAC bands. IRAS 03292+3039 is not detected in IRAC band 1 by the source extraction algorithm but recognized as a faint (1.2 mJy) source with an arc-shaped nebulosity in the images. In addition to these two candidate deeply embedded protostars, two other *IRAS* sources, IRAS 03281+3039 and IRAS 03276+3042, are found in this region. The former was previously classified as a candidate galaxy on the basis of its *IRAS* colors (de Grijp et al. 1987), but it has colors consistent with a Class I YSO in our data. It is located in close proximity to a group of HH filaments, HH 770, 771, and 772 (Walawender et al. 2005) and a group of sources classified as Class II objects in our analysis. It shows strong emission at all IRAC and MIPS wavelengths and

TABLE 5
DEEPLY EMBEDDED OBJECTS/OUTFLOW-DRIVING SOURCES IN PERSEUS WITH IRAC AND MIPS 24 FLUXES

Object	α (J2000.0)	δ (J2000.0)	$S(3.6\ \mu m)$ (mJy)	$S(4.5\ \mu m)$ (mJy)	$S(5.8\ \mu m)$ (mJy)	$S(8.0\ \mu m)$ (mJy)	$S(24\ \mu m)$ (mJy]
L1448-C(N)[a]	03 25 38.9	+30 44 06.0	4.2 ± 0.4	13.5 ± 0.8	11.7 ± 0.8	19.6 ± 1.2	1560 ± 43
L1448-C(S)	03 25 39.1	+30 43 58.9	2.5 ± 0.08	23.6 ± 0.6	77.2 ± 0.8	123 ± 1	[b]
L1448-IRS2	03 25 22.4	+30 45 13.6	0.31 ± 0.02	2.8 ± 0.2	4.5 ± 0.2	10.2 ± 0.1	485 ± 4
L1448-N(A)	03 25 36.5	+30 45 23.2	1.2 ± 0.2	10.5 ± 0.3	43.0 ± 0.5	124 ± 1	3530 ± 104
L1448-N(B)	03 25 36.2	+30 45 17.1	1.6 ± 0.3	4.7 ± 0.5	5.9 ± 0.6	57 ± 2	[b]
B1-a[c]	03 33 16.7	+31 07 55.1	5.4 ± 0.3	50.0 ± 0.6	84.6 ± 0.5	105 ± 0.9	1560 ± 30
B1-b	03 33 20.3	+31 07 21.4	4.1 ± 0.04	16.8 ± 0.1	25.0 ± 0.2	29.6 ± 0.2	164 ± 2
B1-c	03 33 17.9	+31 09 31.8	0.17 ± 0.004	6.6 ± 0.08	34.3 ± 0.2	90.3 ± 0.8	676 ± 10
L1455-IRS1	03 27 39.1	+30 13 02.8	0.64 ± 0.02	8.7 ± 0.2	18.8 ± 0.3	23.3 ± 0.1	1760 ± 34
L1455-IRS4	03 27 43.3	+30 12 28.9	0.76 ± 0.03	3.4 ± 0.1	13.6 ± 0.2	25.0 ± 0.2	761 ± 9
IRAS 03235+3004[c]	03 26 37.5	+30 15 28.2	1.6 ± 0.07	9.9 ± 0.1	11.2 ± 0.08	11.1 ± 0.04	400 ± 3
IRAS 03282+3035	03 31 21.0	+30 45 30.0	0.17 ± 0.006	0.66 ± 0.02	0.64 ± 0.03	0.74 ± 0.02	14.6 ± 0.2
IRAS 03292+3039	03 32 18.2	+30 49 46.9	1.4 ± 0.2	2.3 ± 0.1	2.7 ± 0.07	1.4 ± 0.04	13.1 ± 0.1

NOTES.—For details about the MIPS data see L. Rebull et al. (2006, in preparation). Units of right ascension are hours, minutes, and seconds, and units of declination are degrees, arcminutes, and arcseconds.

[a] L1448-C(N) is also referred to as L1448-C and L1448-mm in the literature, being associated with a strong millimeter source in aperture synthesis observations (see discussion in text).

[b] L1448-C(N) and L1448-C(S) are not separated by the source extraction software at MIPS 24 μm. Likewise for L1448-N(A) and L1448-N(B).

[c] B1-a and IRAS 03235+3004 are detected by 2MASS in the K_s band B1-a with a K_s flux of 1.4 ± 0.1 mJy (upper limits of 0.089 mJy in J and 0.38 mJy in H) and IRAS 03235+3004 with a K_s flux of 1.2 ± 0.08 mJy (upper limits of 0.18 mJy in J and 0.50 mJy in H). None of the remaining sources have 2MASS associations.

is detected in 2MASS, but is not associated with any dust continuum peaks. The latter, IRAS 03276+3042, is likely associated with a candidate Class II source from our catalog also detected at all wavelengths.

6.4. *Colors of Embedded Protostars*

As discussed above, each of the known Class 0 objects discussed above is driving outflows. Table 5 lists the mid-infrared measurements of each of the Class 0 objects, together with the candidate outflow driving sources discussed above. This compilation does not include sources in the areas covered by the guaranteed time observations of NGC 1333 and IC 348 discussed by R. A. Gutermuth et al. (2006, in preparation) and Lada et al. (2006). The detection of mid-infrared counterparts for these deeply embedded protostars nicely demonstrates the high sensitivity of the *Spitzer* observations, since previously only a few deeply embedded protostars had been measured in the mid-infrared. Figure 17 singles these objects out in the [3.6] − [4.5] versus [5.8] − [8.0] diagrams, and Figure 18 shows the SEDs of each of them. Each of these objects would easily be picked out as Class I objects from this diagram with IRAS 03292+3039 at the bluest end of the distribution. These objects actually are somewhat separate from the overall population of Class I objects with in general the reddest colors. It is clear from the diagram that the Class 0 objects have much redder [3.6] − [4.5] colors than [5.8] − [8.0] colors. In the models of Allen et al. (2004) the explanation is that the 10 μm silicate absorption feature overlaps with the IRAC4 (8.0 μm) band. Objects with progressively more massive envelopes will have an increasing silicate absorption feature, and therefore less red [5.8] − [8.0] colors, as the 8.0 μm flux is absorbed. The objects in Figure 17 fall outside the range spanned by the models of embedded YSOs by Allen et al. (2004), with even redder [3.6] − [4.5] colors. Judging from the diagrams of Allen et al. (2004), this could imply larger values of the centrifugal radius (300 AU), which would provide less line-of-sight absorption, similar to the modeling results of the Class 0 protostar IRAS 16293−2422 (Jørgensen et al. 2005). However, we emphasize that this is based on simple one-dimensional models not taking the more detailed source structures into account. Whitney et al. (2003) for example showed that the presence of outflow cavities likewise would lead to bluer colors—although this effect should be important for both [5.8] − [8.0] and [3.6] − [4.5] colors according to the models of Whitney et al. (2003). Additional factors important for these colors could also be that the (proto)stellar photosphere starts dominating at shorter wavelengths: this could cause a double-peaked structure of the SED and can explain the SEDs that have a turnover between the IRAC2 and IRAC3 measurements (Fig. 18). Also, the contribution from the shocked H_2 emission to the 4.5 μm band or deep absorption due to ice features included in the IRAC bands will affect the interpretation of these colors. Combinations of all these effects could be the explanation for the scatter seen in the [5.8] − [8.0] colors of the Class 0 objects in Figure 17. A more detailed dust radiative transfer treatment of the full SED from mid-infrared through (sub)millimeter wavelengths for individual objects is needed to shed further light on these issues.

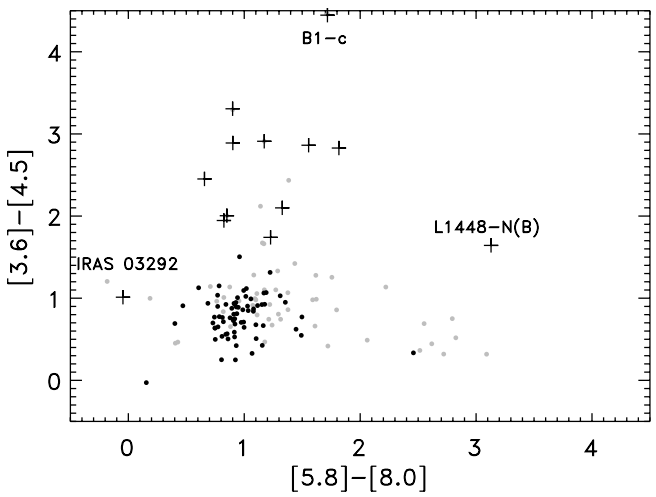

FIG. 17.—Same as the left panel of Fig. 11 (Class I objects with gray and "flat-spectrum" sources with black symbols), but including the candidate deeply embedded protostars (*plus signs*).

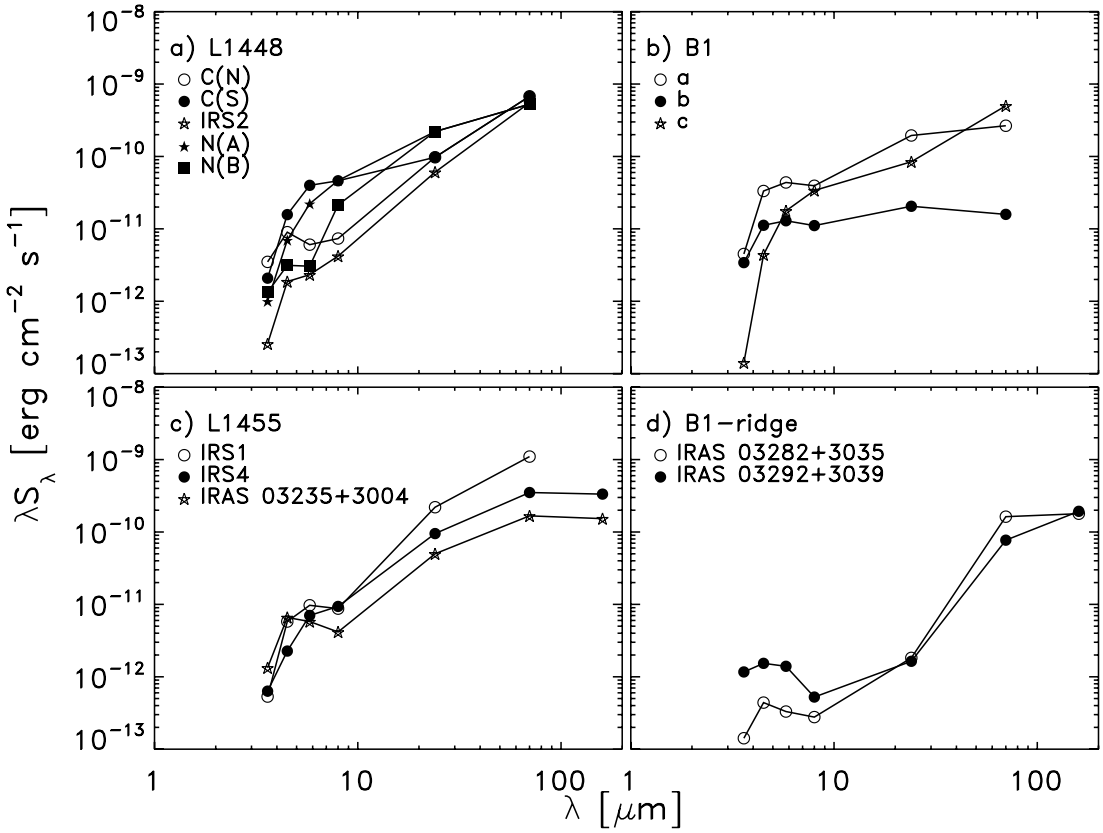

FIG. 18.—Overview of the 3.6–24 μm SEDs for each of the Class 0 objects from Table 5 with additional 70 and 160 μm fluxes from *Spitzer* MIPS observations from c2d (L. Rebull et al. 2006, in preparation). Note that we assume that L1448-C(N) and L1448-C(S), L1448-N(A) and L1448-N(B), respectively, each contribute half of their observed MIPS fluxes and therefore the plotted value for each corresponds to half the number listed in Table 5.

The above discussion also illustrates that some of these potentially very interesting objects may not be singled out directly by the source extraction procedures due to confusion with nearby sources and extended H_2 emission. Of the 13 known protostars listed in Table 5, only five [L1448-C(S), L1455-IRS1, B1-b, B1-c, and IRAS 03235+3004] are included in the high-quality catalog (§ 4.2). It should also be emphasized that the above discussion is not a complete or an exhaustive discussion of all the information available about the outflows in the IRAC maps. For example, information about the shock structure could be obtained by comparing the ratios between the fluxes in different bands. This is outside the scope of this paper, however.

7. SUMMARY

We have presented a survey of 3.86 deg^2 of the Perseus cloud at 3.6, 4.5, 5.8, and 8.0 μm using the *Spitzer Space Telescope* Infrared Array Camera (IRAC). More than 120,000 sources are identified across the field. Based on their mid-infrared colors and comparison to off-cloud and extragalactic control fields, 400 candidate YSOs are identified in this sample. About two-thirds of these YSO candidates are located in two clusters, NGC 1333 and IC 348, constituting 14% of the surveyed area. The YSOs are divided into Class I and II objects using the slope of their SEDs from their 2MASS K_s through IRAC and MIPS 24 μm fluxes: a clear difference is seen with few embedded Class I and "flat-spectrum" YSOs in IC 348 (14% of the YSO population) compared to NGC 1333 (36% of the YSOs) and the remaining, extended cloud (47% of the YSOs). This suggests an evolutionary difference, with NGC 1333 consisting of a younger population of YSOs compared to IC 348 (consistent with previous near-infrared observations), but also that a significant fraction of the current star formation might be going on outside these clusters in the extended cloud where 61% of the Class I objects toward Perseus are found. Finally, we discuss a number of the outflows showing up predominantly through shocked H_2 emission in the IRAC2 maps and identify the mid-infrared counterparts for the deeply embedded Class 0 objects in the region. All known Class 0 objects in Perseus have mid-infrared counterparts. The Class 0 objects are found to have very red [3.6] − [4.5] colors compared to [5.8] − [8.0] colors, but are spread out over a wide range of colors in this diagram.

We are grateful to the staff at the Lorentz Center at Leiden University for hospitality during a three week meeting in 2005 July where a large part of this work was pursued. We thank Mike Dunham for supplying the SHARC II image of the L1455 region. This research has made use of the SIMBAD database, operated at CDS, Strasbourg, France. The research of J. K. J. was supported by NASA Origins Grant NAG5-13050. Support for this work, part of the *Spitzer* Legacy Science Program, was also provided by NASA through contract 1224608, 1230782, and 1230779 issued by the Jet Propulsion Laboratory, California Institute of Technology, under NASA contract 1407. Astrochemistry in Leiden is supported by a NWO Spinoza grant and a NOVA grant. K. E. Y. was supported by NASA under grant NGT5-50401 ussed through the Office of Space Science. The SHARC II data were obtained with support from NASA Origins grant NNG04GG24G to N. J. E.

REFERENCES

Allen, L. E., et al. 2004, ApJS, 154, 363
Andersson, B.-G., Wannier, P. G., Moriarty-Schieven, G. H., & Bakker, E. J. 2000, AJ, 119, 1325
André, P., & Montmerle, T. 1994, ApJ, 420, 837
André, P., Ward-Thompson, D., & Barsony, M. 1993, ApJ, 406, 122
Bally, J., Devine, D., Alten, V., & Sutherland, R. S. 1997, ApJ, 478, 603
Bontemps, S., Andre, P., Terebey, S., & Cabrit, S. 1996, A&A, 311, 858
Cambrésy, L., Petropoulou, V., Kontizas, M., & Kontizas, E. 2006, A&A, 445, 999
Černis, K. 1990, Ap&SS, 166, 315
Dame, T. M., Hartmann, D., & Thaddeus, P. 2001, ApJ, 547, 792
Davis, C. J., Eisloeffel, J., Ray, T. P., & Jenness, T. 1997, A&A, 324, 1013
de Grijp, M. H. K., Lub, J., & Miley, G. K. 1987, A&AS, 70, 95
de Zeeuw, P. T., Hoogerwerf, R., de Bruijne, J. H. J., Brown, A. G. A., & Blaauw, A. 1999, AJ, 117, 354
Enoch, M., et al. 2006, ApJ, 638, 293
Evans, N. J., et al. 2003, PASP, 115, 965
———. 2005, Delivery of Data from the c2d Legacy Project: IRAC and MIPS (Pasadena: SSC)
Fiedler, R., Pauls, T., Johnston, K. J., & Dennison, B. 1994, ApJ, 430, 595
Froebrich, D. 2005, ApJS, 156, 169
Goldsmith, P. F., Snell, R. L., Hemeon-Heyer, M., & Langer, W. D. 1984, ApJ, 286, 599
Greene, T. P., Wilking, B. A., Andre, P., Young, E. T., & Lada, C. J. 1994, ApJ, 434, 614
Gutermuth, R. A., Megeath, S. T., Muzerolle, J., Allen, L. E., Pipher, J. L., Myers, P. C., & Fazio, G. G. 2004, ApJS, 154, 374
Harvey, P., et al. 2006, ApJ, in press
Hatchell, J., Richer, J. S., Fuller, G. A., Qualtrough, C. J., Ladd, E. F., & Chandler, C. J. 2005, A&A, 440, 151
Hirano, N., Kamazaki, T., Mikami, H., Ohashi, N., & Umemoto, T. 1999, in Star Formation 1999, ed. T. Nakamoto (Nobeyama: Nobeyama Radio Obs.), 181
Indebetouw, R., et al. 2005, ApJ, 619, 931
Jørgensen, J. K., et al. 2005, ApJ, 631, L77
Juan, J., Bachiller, R., Koempe, C., & Martin-Pintado, J. 1993, A&A, 270, 432
Lada, C. J. 1987, in IAU Symp. 115, Star-Forming Regions, ed. M. Peimbert & J. Jugaku (Dordrecht: Reidel), 1
Lada, C. J., Alves, J., & Lada, E. A. 1996, AJ, 111, 1964
Lada, C. J., et al. 2006, AJ, 131, 1574
Lada, E. A., & Lada, C. J. 1995, AJ, 109, 1682
Ladd, E. F., Lada, E. A., & Myers, P. C. 1993, ApJ, 410, 168
Looney, L. W., Mundy, L. G., & Welch, W. J. 2000, ApJ, 529, 477
Luhman, K. L., Stauffer, J. R., Muench, A. A., Rieke, G. H., Lada, E. A., Bouvier, J., & Lada, C. J. 2003, ApJ, 593, 1093
Matthews, B. C., & Wilson, C. D. 2002, ApJ, 574, 822
Megeath, S. T., et al. 2004, ApJS, 154, 367
Muzerolle, J., et al. 2004, ApJS, 154, 379
O'Linger, J., Wolf-Chase, G., Barsony, M., & Ward-Thompson, D. 1999, ApJ, 515, 696
Padoan, P., Bally, J., Billawala, Y., Juvela, M., & Nordlund, A. 1999, ApJ, 525, 318
Ridge, N. A., et al. 2006, ApJ, 643, 932
Sargent, A. I. 1979, ApJ, 233, 163
Schnee, S. L., Ridge, N. A., Goodman, A. A., & Li, J. G. 2005, ApJ, 634, 442
Wainscoat, R. J., Cohen, M., Volk, K., Walker, H. J., & Schwartz, D. E. 1992, ApJS, 83, 111
Walawender, J., Bally, J., Kirk, H., & Johnstone, D. 2005, AJ, 130, 1795
Walawender, J., Bally, J., Reipurth, B., & Aspin, C. 2004, AJ, 127, 2809
Whitney, B. A., Wood, K., Bjorkman, J. E., & Wolff, M. J. 2003, ApJ, 591, 1049
Wilking, B. A., Meyer, M. R., Greene, T. P., Mikhail, A., & Carlson, G. 2004, AJ, 127, 1131
Young, K. E., et al. 2005, ApJ, 628, 283